J. Fluid Mech. (2010), *vol.* 661, *pp.* 482–510.
doi:10.1017/S002211201000306X

Discrete particle simulation of particle–fluid flow: model formulations and their applicability

Z. Y. ZHOU, S. B. KUANG, K. W. CHU
AND A. B. YU†

Laboratory for Simulation and Modelling of Particulate Systems, School of Materials Science and Engineering, The University of New South Wales, Sydney NSW 2052, Australia

(Received 3 September 2009; revised 28 May 2010; accepted 28 May 2010;

The approach of combining computational fluid dynamics (CFD) for continuum fluid and the discrete element method (DEM) for discrete particles has been increasingly used to study the fundamentals of coupled particle–fluid flows. Different CFD–DEM models have been used. However, the origin and the applicability of these models are not clearly understood. In this paper, the origin of different model formulations is discussed first. It shows that, in connection with the continuum approach, three sets of formulations exist in the CFD–DEM approach: an original format set I, and subsequent derivations of set II and set III, respectively, corresponding to the so-called model A and model B in the literature. A comparison and the applicability of the three models are assessed theoretically and then verified from the study of three representative particle–fluid flow systems: fluidization, pneumatic conveying and hydrocyclones. It is demonstrated that sets I and II are essentially the same, with small differences resulting from different mathematical or numerical treatments of a few terms in the original equation. Set III is however a simplified version of set I. The testing cases show that all the three models are applicable to gas fluidization and, to a large extent, pneumatic conveying. However, the application of set III is conditional, as demonstrated in the case of hydrocyclones. Strictly speaking, set III is only valid when fluid flow is steady and uniform. Set II and, in particular, set I, which is somehow forgotten in the literature, are recommended for the future CFD–DEM modelling of complex particle–fluid flow.

Key words: fluidized beds, granular media, particle–fluid flows

1. Introduction

Coupled particle–fluid flow can be observed in almost all types of particulate processes which are widely used in industry. Understanding the fundamentals governing the flow and formulating suitable governing equations and constitutive relationships are of paramount importance to the formulation of strategies for process development and control. This necessitates a multi-scale approach to understanding the phenomena at different time and length scales (see e.g. Villermaux 1996; Xu & Yu 1997; Li 2000; Tsuji 2007; Zhu *et al.* 2007). The existing approaches to modelling particle flow can generally be classified into two categories: the continuum approach at a macroscopic level and the discrete approach at a microscopic level. In the

---

† Email address for correspondence: a.yu@unsw.edu.au

continuum approach, the macroscopic behaviour is described by balance equations, e.g. mass and momentum, closed with constitutive relations together with initial and boundary conditions (see e.g. Anderson & Jackson 1967; Ishii 1975; Gidaspow 1994; Enwald, Peirano & Almstedt 1996). The discrete approach is based on the analysis of the motion of individual particles, i.e. typically by means of the discrete element method (DEM) (Cundall & Strack 1979). The method considers a finite number of discrete particles interacting by means of contact and non-contact forces, and every particle in a considered system is described by Newton's equations of motion. On the other hand, fluid flow can be modelled at different time and length scales from discrete (e.g. molecular dynamic simulation, lattice Boltzman, pseudo-particle method) to continuum (direct numerical simulation, large-eddy simulation and other conventional computational fluid dynamics (CFD) techniques). Different combinations of models for the particle phase and fluid phase can be made, and their relative merits in describing particle–fluid flow have been discussed (see e.g. Yu 2005; Zhu *et al.* 2007).

Two popular combinations are widely used to describe particle–fluid flow: the two-fluid model (TFM) and CFD–DEM. In TFM, both fluid and solid phases are treated as interpenetrating continuum media in a computational cell which is much larger than individual particles but still small compared with the size of process equipment (Anderson & Jackson 1967). However, its effective use heavily depends on the constitutive or closure relations for the solid phase and the momentum exchange between phases, which are often difficult to obtain within its framework; this is particularly true when dealing with different types of particles that should be treated as different phases. In CFD–DEM, the motion of discrete particles is obtained by solving Newton's second law of motion as used in DEM, and the flow of continuum fluid by solving the Navier–Stokes equations based on the concept of local average as used in CFD, with the coupling of CFD and DEM through particle–fluid interaction forces (Xu & Yu 1997). The main advantage of CFD–DEM is that it can generate detailed particle-scale information, such as the trajectories of and forces acting on individual particles, which is key to elucidating the mechanisms governing the complicated flow behaviour. With the rapid development of computer technology, the CFD–DEM approach has been increasingly used by various investigators to study various particle–fluid flow systems as, for example, reviewed by Zhu *et al.* (2007, 2008).

The implementation of a CFD–DEM model, as pointed out by Feng & Yu (2004*a*), lies in three aspects: the formulation of governing equations, the coupling scheme for numerical computation and the calculation of particle–fluid interaction forces. The latter two have been well discussed, particularly for monosized particles (Feng & Yu 2004*a*; Zhu *et al.* 2007). However, the first aspect is not well established. In fact, two models, called model A and model B, have been used by different investigators, and there are conflicting views regarding their applications (Hoomans *et al.* 1998; Xu & Yu 1998; Kafui, Thornton & Adams 2002, 2004; Feng & Yu 2004*a*,*b*; Di Renzo & Di Maio 2007). Xu & Yu (1998) pointed out that the interpretation of the fluid–particle interaction force is different for both models, but both the methods can meet the requirement that the bed pressure drop balances the bed weight at minimum fluidization and hence are valid for fluidization. Kafui *et al.* (2002) discussed model A and model B, and summarized the models used by different research groups. Nevertheless, their claim that model A best captures the essential features of a fixed/fluidized bed was questionable, as noted by Feng & Yu (2004*b*) and Kafui *et al.* (2004). It is now clear that the two models have little significant difference when applied to gas fluidization of monosized particles. It is not clear which is better when applied to the modelling of fluidization of particle mixtures, but this problem is related to the calculation of particle–fluid interaction forces. In fact, how to calculate the fluid drag force acting on a particle in a mixture is still an open problem (Feng & Yu 2004*a*; Beetstra, van der Hoef & Kuipers 2007). More recently, the two models were further discussed by Di Renzo & Di Maio (2007). These authors claimed that model B is only valid at the minimum fluidization condition, contrary to those by other investigators (Kafui *et al.* 2004; Feng & Yu 2004*b*). Therefore, although the CFD–DEM approach is now widely used, its theoretical background is not fully established. In fact, to date, there are still some basic questions which need to be answered. For example, what are the origins of different models such as model A and model B? What are the exact differences between those models? What is the applicability or limitation of a particular model, and which model is the most appropriate for modelling different particle–fluid flow systems?

This paper provides our answers to those questions. Firstly, the origins of different formulations in the continuum approach are explored. It is argued that three models, rather than two, exist in the continuum approach. Then, it is demonstrated that corresponding to the continuum approach, there are three models in the CFD–DEM approach. The relationships between the three models are discussed, and their applicability is analysed theoretically and verified in a comparative study of three representative particle–fluid flow systems: fluidization, pneumatic conveying and hydrocyclones.

2. Theoretical treatments

2.1. *Origin of different model formulations in the continuum approach*

The model formulation in the continuum approach to describing particle–fluid flow, focused on gas–solid flow in fluidization, has been proposed since the 1960s, including those, for example, by Anderson & Jackson (1967), Ishii (1975), Gidaspow (1994), Enwald *et al.* (1996) and Jackson (1997). In practice, different sets of governing equations from different resources have been used (e.g. Arastoopour & Gidaspow 1979; Lee & Lyczkowski 2000; van Wachem *et al.* 2001). However, the area has been well established, as recently summarized by Prosperetti & Tryggvason (2007). Unfortunately, this is not the case in the CFD–DEM approach, as described in § 1. On the other hand, the derivation of CFD–DEM models is closely related to the continuum approach due to the fact that fluid flow is still modelled at the macroscopic local average level. Thus, it is helpful to start our discussion with the TFM approach.

In the continuum approach, both fluid and solid phases are treated as continuous media. Anderson & Jackson (1967) used the local average method to directly derive the fluid governing equation on the basis of the point equation of motion of the fluid, and the solid phase governing equation on the basis of the equation of motion for the centre of mass of a single particle. They obtained the first set of governing equations (set I):

$$\rho_f\varepsilon_f[\partial(\boldsymbol{u})/\partial t + \nabla\cdot(\boldsymbol{uu})] = \nabla\cdot\boldsymbol{\xi} - n\boldsymbol{f}_i + \rho_f\varepsilon_f\boldsymbol{g} \quad \text{(fluid phase)}, \tag{2.1}$$

$$\rho_s\varepsilon_s[\partial(\boldsymbol{v})/\partial t + \nabla\cdot(\boldsymbol{vv})] = n\boldsymbol{\Phi} - \nabla\cdot\boldsymbol{S} + n\boldsymbol{f}_i + \rho_s\varepsilon_s\boldsymbol{g} \quad \text{(solid phase)}, \tag{2.2}$$

where ε_f and $\varepsilon_s(= 1 - \varepsilon_f)$ are, respectively, volume fractions of fluid and particles. $\boldsymbol{\xi}$ is fluid stress tensor, $\boldsymbol{\Phi}$ is the local mean value of particle–particle interaction force, $\boldsymbol{S}$ is the tensor representing 'Reynolds stresses' for the particle phase, $\boldsymbol{f}_i$ is the local mean value of the force on particle i by its surrounding fluid and n is the number of particles per unit volume. This cannot be used unless the undetermined terms or dependency of $\boldsymbol{\xi}$, $\boldsymbol{\Phi}$, $\boldsymbol{S}$ and $\boldsymbol{f}_i$ on the voidage, the local mean velocities and the pressure are known. In order to solve the problem, Anderson & Jackson (1967) derived some constitutive equations, including: (i) combination of $n\boldsymbol{\Phi}$ and $-\nabla\cdot\boldsymbol{S}$ into $-\nabla\cdot\boldsymbol{\xi}^s$ which represents the solid stress tensor; (ii) $\boldsymbol{\xi}$ and $\boldsymbol{\xi}^s$ are analogous to that for the stress tensor in a Newtonian fluid, and written into $\boldsymbol{\xi} = -p\boldsymbol{\delta}_{\boldsymbol{k}} + f(\lambda, \mu, \boldsymbol{u})$, where p is the local mean fluid pressure and λ, μ are, respectively, the effective bulk and shear viscosities; and (iii) decomposition of $n\boldsymbol{f}_i$ into two components, namely, a component due to 'macroscopic' variations in the fluid stress tensor on a large scale compared with the particle spacing, together with the other component representing the effect of detailed variations of the point stress tensor as the fluid flows around a particle. That is,

$$n\boldsymbol{f}_i = n(V_p\nabla\cdot\boldsymbol{\xi})/\Delta V + n\boldsymbol{f}'_i = \varepsilon_s\nabla\cdot\boldsymbol{\xi} + n\boldsymbol{f}'_i, \tag{2.3}$$

where V_p is the volume of the particle and $n\boldsymbol{f}'_i$ represents the part of the total fluid–particle interaction force per unit bed volume arising from the detailed variations in the stress tensor induced by fluctuations in velocity as the fluid passes around individual particles and through the interstices between particles. It mainly includes the drag force in the direction of the relative velocity $(\boldsymbol{u}_i - \boldsymbol{v}_i)$, and virtual mass force proportional to the mass of fluid displaced by a particle. Other forces such as the lift force can also be included. Thus, the interaction force $n\boldsymbol{f}_i$ in (2.1) and (2.2) is replaced by (2.3) together with the consideration of $n\boldsymbol{\Phi}-\nabla\cdot\boldsymbol{S} = -\nabla\cdot\boldsymbol{\xi}^s$, giving the second set of equations (set II):

$$\rho_f\varepsilon_f[\partial(\boldsymbol{u})/\partial t + \nabla\cdot(\boldsymbol{uu})] = \varepsilon_f\nabla\cdot\boldsymbol{\xi} - n\boldsymbol{f}'_i + \rho_f\varepsilon_f\boldsymbol{g} \quad \text{(fluid phase)}, \tag{2.4}$$

$$\rho_s\varepsilon_s[\partial(\boldsymbol{v})/\partial t + \nabla\cdot(\boldsymbol{vv})] = \varepsilon_s\nabla\cdot\boldsymbol{\xi} + n\boldsymbol{f}'_i + \rho_s\varepsilon_s\boldsymbol{g} + \nabla\cdot\boldsymbol{\xi}^s \quad \text{(solid phase)}. \tag{2.5}$$

On comparing the governing equations in sets I and II, it can be seen that the difference is caused by the introduction of those constitutive equations. Anderson & Jackson (1967) commented that set I is derived directly from the basic equations of fluid mechanics for the system, the subsequent set II reflects their own opinion of the most appropriate form for the undermined terms in set I.

Based on set II, particle–fluid interaction force can be further written in another format (Jackson 1963; Anderson & Jackson 1967). In particular, to eliminate the fluid stress tensor term, an equation is obtained by multiplying (2.5) by $(1 - \varepsilon_f)/\varepsilon_f$ and subtracting from (2.4), giving

$$\rho_s\varepsilon_s[\partial(\boldsymbol{v})/\partial t + \nabla\cdot(\boldsymbol{vv})] = n\boldsymbol{f}'_i/\varepsilon_f - \rho_f\varepsilon_s\boldsymbol{g} + \rho_f\varepsilon_s[\partial(\boldsymbol{u})/\partial t + \nabla\cdot(\boldsymbol{uu})] + \rho_s\varepsilon_s\boldsymbol{g} + \nabla\cdot\boldsymbol{\xi}^s. \tag{2.6}$$

This is an equation of motion for particles which does not contain the fluid stress tensor $\boldsymbol{\xi}$. When compared with (2.5), it can be seen that the elimination of fluid stress tensor $\boldsymbol{\xi}$ has introduced a buoyancy term $(-\rho_f\varepsilon_s\boldsymbol{g})$ and a term $\rho_f\varepsilon_s$ $[\partial(\boldsymbol{u})/\partial t + \nabla\cdot(\boldsymbol{uu})]$ which represents the fluid acceleration into the particle equation of motion. The magnitude of the fluid acceleration term depends on flow conditions. If this term approaches zero or much smaller than $(n\boldsymbol{f}'_i/\varepsilon_f - \rho_f\varepsilon_s\boldsymbol{g})$, according to (2.6), the total particle–fluid interaction force acting on particles can be written as

$$n\boldsymbol{f}_i = n\boldsymbol{f}'_i/\varepsilon_f - \rho_f\varepsilon_s\boldsymbol{g}. \tag{2.7}$$

Incorporating (2.7) into (2.1) and (2.2) and considering $n\boldsymbol{\Phi} - \nabla\cdot\boldsymbol{S} = -\nabla\cdot\boldsymbol{\xi}^s$ give the third set of governing equations (set III):

$$\rho_f\varepsilon_f[\partial(\boldsymbol{u})/\partial t + \nabla\cdot(\boldsymbol{uu})] = \nabla\cdot\boldsymbol{\xi} - [n\boldsymbol{f}'_i/\varepsilon_f - \rho_f\varepsilon_s\,\boldsymbol{g}] + \rho_f\varepsilon_f\boldsymbol{g} \quad \text{(fluid phase)}, \tag{2.8}$$

$$\rho_s\varepsilon_s[\partial(\boldsymbol{v})/\partial t + \nabla\cdot(\boldsymbol{vv})] = \nabla\cdot\boldsymbol{\xi}^s + [n\boldsymbol{f}'_i/\varepsilon_f - \rho_f\varepsilon_s\,\boldsymbol{g}] + \rho_s\varepsilon_s\,\boldsymbol{g} \quad \text{(solid phase)}. \tag{2.9}$$

However, it should be pointed out that the derivation of this set of equations is conditional. Strictly speaking, the following conditions for the fluid phase should be satisfied:

$$\rho_f\varepsilon_s[\partial(\boldsymbol{u})/\partial t + \nabla\cdot(\boldsymbol{uu})] = 0. \tag{2.10}$$

This indicates that the fluid flow through the particle phase should be steady and uniform (Anderson & Jackson 1967; Gidaspow 1994).

On the other hand, hydrodynamics models with concepts of the so-called models A and B have been widely used for the particle–fluid flow, as discussed by Bouillard, Lyczkowski & Gidaspow (1989), and later by Gidaspow (1994) and Enwald *et al.* (1996). The difference between models A and B depends on the treatment of the pressure source term in the governing equations. Generally speaking, if the pressure is attributed to the fluid phase alone, it is referred to as model B. If the pressure is shared by both the fluid and solid phases, it is referred to as model A. Bouillard *et al.* (1989) attributed the origin of model A to Nakamura & Capes (1973) and Lee & Lyczkowski (1981), and that of model B to Rudinger & Chang (1964) and Lyczkowski (1978). The drag coefficients β_A and β_B are, respectively, defined in models A and B to calculate the particle–fluid interaction force. The applications of those two sets of governing equations and their comparison have been assessed for pneumatic conveying (Arastoopour & Gidaspow 1979) and fluidization process (Bouillard *et al.* 1989), showing insignificant difference between the two models. Bouillard *et al.* (1989) commented that the main problem with model A is its stability, and being conditional on the absence of all viscous stresses and without the solid elastic modulus $\boldsymbol{g}(\varepsilon_f)$, while model B, which possesses all real characteristics, makes the set of equations well-posed. But Enwald *et al.* (1996) later clarified that nobody has yet proved well-posedness for a multi-dimensional initial-boundary value problem. To date, most researchers prefer model A, as reflected by the fact that commercial software packages FLUENT and CFX both use model A.

On comparing the three formulations (sets I, II and III) with those hydrodynamics models A and B, it can be seen that in principle, model A is consistent with set II, and model B with set III. However, sets II and III are more general than models A and B but less detailed, which is another reason why the concepts of models A and B are more popular in TFM modelling. Mathematically, sets I and II (model A) are identical, as seen from the derivation of set II. Set III (or model B) is a simplified form of set I with the assumption of (2.10). It should be noted that, according to the definition of model B, set I is also in a form of model B. Thus, model B has two types: an original model B (set I) and a simplified model B. The deficiency of simplified model B has been realized by some investigators (e.g. Anderson & Jackson 1967; Gidaspow 1994). However, the difference between original model B and simplified model B has not been fully recognized, and the original model B (set I) is somehow forgotten. The two models are mixed up, and only simplified model B is commonly used. This has created some conceptual problems. For example, although model B or its treatment is argued to be well-posed, model A, which may be ill-posed, is more widely used due to its convenience in numerical implementation. When applied to CFD–DEM modelling, some investigators feel that the model B treatment is better than model A. However, because a simplified model B was used, the treatment experiences problems, as discussed in § 2.3.

Nevertheless, the governing equations in the continuum approach have been well established, particularly if the expressions for different source terms are ignored. The challenge remaining is to develop closure laws to determine solid flow parameters including dynamic/bulk viscosities and particle pressure, and interfacial momentum transfer in multi-sized system (Bouillard *et al.* 1989; Enwald *et al.* 1996; Arastoopour 2001; van Wachem *et al.* 2001). Two approaches are commonly used to achieve this goal. One is to formulate empirical models mainly based on particle properties and (local) voidage. However, those models vary significantly, depending on the conditions, as reviewed by Enwald *et al.* (1996). The other way is to use the so-called kinetic theory (e.g. Gidaspow 1994; Iddir, Arastoopour & Hrenya 2005). However, its general application is still questioned (see e.g. Campbell 2006; Goldhirsch 2008). Particles exhibit three flow regimes: quasi-static, fast and in-between; to date, the success of TFM is largely limited to the fast flow regime. This difficulty does not exist in the CFD–DEM approach, as discussed below.

2.2. *Model formulations in the computational fluid dynamics–discrete element method approach*

Corresponding to the three set models in the continuum approach, CFD–DEM also has three models. However, the CFD–DEM approach is quite different from the traditional TFM. In CFD–DEM, one has to consider the coupling between DEM at the particle scale and CFD at the computational cell scale. The main difference between the CFD–DEM and TFM approaches lies in the treatment of the particle phase. In CFD–DEM, for the particle phase, based on the soft sphere model originally proposed by Cundall & Strack (1979), a particle in a particle–fluid flow system can have two types of motion: translational and rotational. The governing equations for the translational and rotational motion of particle i with radius R_i, mass m_i and moment of inertia I_i can be written as

$$m_i \frac{\mathrm{d}\boldsymbol{v}_i}{\mathrm{d}t} = \boldsymbol{f}_{pf,i} + \sum_{j=1}^{k_c} (\boldsymbol{f}_{c,ij} + \boldsymbol{f}_{d,ij}) + m_i \boldsymbol{g}, \tag{2.11}$$

$$I_i \frac{\mathrm{d}\boldsymbol{\omega}_i}{\mathrm{d}t} = \sum_{j=1}^{k_c} (\boldsymbol{M}_{t,ij} + \boldsymbol{M}_{r,ij}), \tag{2.12}$$

where $\boldsymbol{v}_i$ and $\boldsymbol{\omega}_i$ are, respectively, the translational and angular velocities of the particle, and k_c is the number of particles in interaction with the particle. The forces involved are: the particle–fluid interaction force $\boldsymbol{f}_{pf,i}$, the gravitational force $m_i\boldsymbol{g}$, and inter-particle forces between particles which include the elastic force $\boldsymbol{f}_{c,ij}$ and viscous damping force $\boldsymbol{f}_{d,ij}$. The torque acting on particle i by particle j includes two components: $\boldsymbol{M}_{t,ij}$, generated by the tangential force, and $\boldsymbol{M}_{r,ij}$, commonly known as the rolling friction torque. The equations used to calculate the particle–particle interaction forces and torques have been well established in the literature (Zhu *et al.* 2007). Many of these have been used in our previous studies of particle–fluid flow (Xu & Yu 1997; Zhou *et al.* 1999; Xu *et al.* 2000; Feng & Yu 2004*a*; Feng *et al.* 2004; Feng & Yu 2007; Chu & Yu 2008; Kuang *et al.* 2008; Zhou, Yu & Zulli 2009).

The particle–fluid interaction force $\boldsymbol{f}_{pf}$, similar to $\boldsymbol{f}_i$ in the continuum approach, is the sum of all types of particle–fluid interaction forces acting on individual particles by fluid, including the so-called drag force $\boldsymbol{f}_d$, pressure gradient force $\boldsymbol{f}_{\nabla p}$, viscous force $\boldsymbol{f}_{\nabla\cdot\boldsymbol{\tau}}$ due to the fluid shear stress or deviatoric stress tensor, virtual mass force $\boldsymbol{f}_{vm}$, Basset force $\boldsymbol{f}_B$ and lift forces such as the Saffman force $\boldsymbol{f}_{Saff}$ and Magnus force $\boldsymbol{f}_{Mag}$ (Crowe, Sommerfeld & Tsuji 1998). Unless otherwise specified in later discussion, the buoyancy force is included in the pressure gradient force $\boldsymbol{f}_{\nabla p}$. Therefore, the total particle–fluid interaction force on an individual particle i can be written as

$$\boldsymbol{f}_{pf,i} = \boldsymbol{f}_{d,i} + \boldsymbol{f}_{\nabla p,i} + \boldsymbol{f}_{\nabla\cdot\boldsymbol{\tau},i} + \boldsymbol{f}_{vm,i} + \boldsymbol{f}_{B,i} + \boldsymbol{f}_{Saff,i} + \boldsymbol{f}_{Mag,i}. \tag{2.13}$$

Many correlations have been proposed to calculate the particle–fluid interaction forces, particularly the drag force which can be based on the equation of Ergun (1952) and Wen & Yu (1966) equations, and correlation of Di Felice (1994) or others. Details of those correlations can be found elsewhere (e.g. Crowe *et al.* 1998; Zhu *et al.* 2007).

For the fluid phase, its flow is essentially governed by the Navier–Stokes equation to be satisfied at every point of the fluid. As discussed earlier, the present interest is more focused on the particle behaviour, not fluid phase. The flow of fluid can thus be determined at a large scale, such as a CFD cell, which may contain many particles. Consequently, the governing equations for fluid phase are obtained based on the local averaged method as used in TFM. The fluid governing equations corresponding to sets I, II and III are summarized in table 1. Note that the equations to calculate the volumetric particle–fluid interaction force $\boldsymbol{F}_{pf}$ differ for different sets, although they are all related to the particle–fluid interaction force $\boldsymbol{f}_{pf}$.

It should be noted that $\boldsymbol{\tau} = \mu[\nabla\boldsymbol{u} + (\nabla\boldsymbol{u})^{-1}] - (2/3)\mu(\nabla\cdot\boldsymbol{u})\boldsymbol{\delta}_k$ for Newtonian fluids. Corresponding to the volumetric particle–fluid interaction force terms in sets I, II and III, those force terms in (2.15)–(2.17) are respectively written by $\boldsymbol{F}_{pf}^{\mathrm{set\,I}}(= n\boldsymbol{f}_i)$, $\boldsymbol{F}_{pf}^{\mathrm{set\,II}}(= n\boldsymbol{f}'_i)$ and $\boldsymbol{F}_{pf}^{\mathrm{set\,III}}(= n\boldsymbol{f}'_i/\varepsilon_f - \rho_f\varepsilon_s\boldsymbol{g})$. The definitions of $n\boldsymbol{f}_i$ and $n\boldsymbol{f}'_i$ can be found in § 2.1, and their determination in CFD–DEM is described below.

The coupling of CFD and DEM is achieved mainly through the particle–fluid interaction force, which is at the computational cell level for the fluid phase ($\boldsymbol{F}_{pf}$ in (2.15)–(2.17)) and at the individual particle level for the solid phase ($\boldsymbol{f}_{pf}$ in (2.13)). Three coupling schemes have been identified (Feng & Yu 2004*a*). In scheme 1, the force on the fluid phase from particles is calculated by a local-average method as used in the TFM, whereas the force on a particle from the fluid phase is calculated separately according to individual particle velocity. In scheme 2, the force on the fluid phase from particles is first calculated at a local-average scale as used in scheme 1, then this force is distributed among individual particles according to a certain average rule. In scheme 3, at each time step, the particle–fluid interaction forces on individual particles in a computational cell are calculated first, and the values are then summed to produce the particle–fluid interaction force at the cell scale. Theoretically, scheme 1 is problematic because Newton's third law of motion may not hold in describing the particle–fluid interaction. This problem is not there for schemes 2 and 3, but the implementation of scheme 2 needs to introduce an extra assumption or numerical treatment at a CFD cell level to distribute the particle–fluid forces among the particles in the cell. Because scheme 3 represents the basic features of CFD–DEM modelling from particle scale to computational cell scale, it is more reasonable and logical. In fact, it has been widely used since its introduction by Xu & Yu (1997). Thus, the total volumetric particle–fluid interaction force $n\boldsymbol{f}_i$ in a computational cell of volume ΔV

Mass conservation: $\partial(\varepsilon_f)/\partial t + \nabla\cdot(\varepsilon_f \boldsymbol{u}) = 0.$ (2.14)

Momentum conservation (and corresponding particle–fluid interaction force).

Set I:

$$\partial(\rho_f \varepsilon_f \boldsymbol{u})/\partial t + \nabla\cdot(\rho_f \varepsilon_f \boldsymbol{u}\boldsymbol{u}) = -\nabla p - \boldsymbol{F}_{pf}^{\text{set I}} + \nabla\cdot\boldsymbol{\tau} + \rho_f \varepsilon_f \boldsymbol{g}, \tag{2.15a}$$

$$\text{where} \quad \boldsymbol{F}_{pf}^{\text{set I}} = \frac{1}{\Delta V}\sum_{i=1}^{n}\left(\boldsymbol{f}_{d,i} + \boldsymbol{f}_{\nabla p,i} + \boldsymbol{f}_{\nabla\cdot\boldsymbol{\tau},i} + \boldsymbol{f}_i''\right),$$

$$\text{and} \quad \boldsymbol{f}_{pf,i} = \boldsymbol{f}_{d,i} + \boldsymbol{f}_{\nabla p,i} + \boldsymbol{f}_{\nabla\cdot\boldsymbol{\tau},i} + \boldsymbol{f}''. \tag{2.15b}$$

Set II:

$$\partial(\rho_f \varepsilon_f \boldsymbol{u})/\partial t + \nabla\cdot(\rho_f \varepsilon_f \boldsymbol{u}\boldsymbol{u}) = -\varepsilon_f \nabla p - \boldsymbol{F}_{pf}^{\text{set II}} + \varepsilon_f \nabla\cdot\boldsymbol{\tau} + \rho_f \varepsilon_f \boldsymbol{g}, \tag{2.16a}$$

$$\text{where} \quad \boldsymbol{F}_{pf}^{\text{set II}} = \frac{1}{\Delta V}\sum_{i=1}^{n}\left(\boldsymbol{f}_{d,i} + \boldsymbol{f}_i''\right), \quad \text{and} \quad \boldsymbol{f}_{pf,i} = \boldsymbol{f}_{d,i} + \boldsymbol{f}_{\nabla p,i} + \boldsymbol{f}_{\nabla\cdot\boldsymbol{\tau},i} + \boldsymbol{f}''. \tag{2.16b}$$

Set III:

$$\partial(\rho_f \varepsilon_f \boldsymbol{u})/\partial t + \nabla\cdot(\rho_f \varepsilon_f \boldsymbol{u}\boldsymbol{u}) = -\nabla p - \boldsymbol{F}_{pf}^{\text{set III}} + \nabla\cdot\boldsymbol{\tau} + \rho_f \varepsilon_f \boldsymbol{g}, \tag{2.17a}$$

$$\text{where} \quad \boldsymbol{F}_{pf}^{\text{set III}} = \frac{1}{\varepsilon_f \Delta V}\sum_{i=1}^{n}\left(\boldsymbol{f}_{d,i} + \boldsymbol{f}_i''\right) - \frac{1}{\Delta V}\sum_{i=1}^{n}\left(\rho_f V_{p,i}\boldsymbol{g}\right),$$

$$\text{and} \quad \boldsymbol{f}_{pf,i} = (\boldsymbol{f}_{d,i} + \boldsymbol{f}_i'')/\varepsilon_f - \rho_f V_{p,i}\boldsymbol{g}. \tag{2.17b}$$

Notes. (1) The governing equations for particle phase are given by (2.11) and (2.12).
(2) $\boldsymbol{f}_i'' = \boldsymbol{f}_{vm,i} + \boldsymbol{f}_{B,i} + \boldsymbol{f}_{Saff,i} + \boldsymbol{f}_{Mag,i}$ is the sum of particle–fluid interaction forces on particle i, other than the drag, pressure gradient and viscous forces which are often regarded as the dominant forces in particle–fluid flow.

TABLE 1. Formulations of different models in the CFD–DEM approach.

can be determined by

$$n\boldsymbol{f}_i = \frac{1}{\Delta V}\sum_{i=1}^{n}(\boldsymbol{f}_{pf,i}) = \frac{1}{\Delta V}\sum_{i=1}^{n}(\boldsymbol{f}_{\nabla p,i} + \boldsymbol{f}_{\nabla\cdot\boldsymbol{\tau},i} + \boldsymbol{f}_{d,i} + \boldsymbol{f}_{vm,i} + \boldsymbol{f}_{B,i} + \boldsymbol{f}_{Saff,i} + \boldsymbol{f}_{Mag,i}). \tag{2.18}$$

Equation (2.18) represents the total particle–fluid interaction force in a cell determined at a particle scale. According to (2.3), the total force in a cell in the continuum approach can be further rewritten as

$$n\boldsymbol{f}_i = -\varepsilon_s \nabla p + \varepsilon_s \nabla\cdot\boldsymbol{\tau} + n\boldsymbol{f}_i'. \tag{2.19}$$

Equations (2.18) and (2.19) should be consistent. Then

$$n\boldsymbol{f}_i' = n\boldsymbol{f}_i - (-\varepsilon_s \nabla p + \varepsilon_s \nabla\cdot\boldsymbol{\tau}) = \frac{1}{\Delta V}\sum_{i=1}^{n}(\boldsymbol{f}_{d,i} + \boldsymbol{f}_{vm,i} + \boldsymbol{f}_{B,i} + \boldsymbol{f}_{Saff,i} + \boldsymbol{f}_{Mag,i}). \tag{2.20}$$

Thus, the volumetric particle–fluid interaction force in each model can be written as

$$\boldsymbol{F}_{pf}^{\text{set I}} = n\boldsymbol{f}_i = \frac{1}{\Delta V}\sum_{i=1}^{n}(\boldsymbol{f}_{\nabla p,i} + \boldsymbol{f}_{\nabla\cdot\boldsymbol{\tau},i} + \boldsymbol{f}_{d,i} + \boldsymbol{f}_{vm,i} + \boldsymbol{f}_{B,i} + \boldsymbol{f}_{Saff,i} + \boldsymbol{f}_{Mag,i}), \tag{2.21}$$

$$\boldsymbol{F}_{pf}^{\text{set II}} = n\boldsymbol{f}_i' = \frac{1}{\Delta V}\sum_{i=1}^{n}(\boldsymbol{f}_{d,i} + \boldsymbol{f}_{vm,i} + \boldsymbol{f}_{B,i} + \boldsymbol{f}_{Saff,i} + \boldsymbol{f}_{Mag,i}), \tag{2.22}$$

$$\boldsymbol{F}_{pf}^{\text{set III}} = n\boldsymbol{f}_i'/\varepsilon_f - \rho_f\varepsilon_s\,\boldsymbol{g} = \frac{1}{\varepsilon_f\Delta V}\sum_{i=1}^{n}(\boldsymbol{f}_{d,i} + \boldsymbol{f}_{vm,i} + \boldsymbol{f}_{B,i} + \boldsymbol{f}_{Saff,i} + \boldsymbol{f}_{Mag,i}) - \frac{1}{\Delta V}\sum_{i=1}^{n}(\rho_f V_{p,i}\,\boldsymbol{g}). \tag{2.23}$$

When coupling CFD with DEM, or *vice versa*, the governing equations should be consistent, as noted by Xu & Yu (1998). Generally speaking, for all the three models, the governing equations for particles can be the same, shown in (2.11)–(2.13). However, in order to satisfy the Newton's third law of motion, for set III, the particle–fluid interaction force acting on particles, instead of (2.13), can be obtained from (2.23), and written as

$$\boldsymbol{f}_{pf,i} = \frac{1}{\varepsilon_f}\left(\boldsymbol{f}_{d,i} + \boldsymbol{f}_{vm,i} + \boldsymbol{f}_{B,i} + \boldsymbol{f}_{Saff,i} + \boldsymbol{f}_{Mag,i}\right) - \rho_f V_{p,i}\boldsymbol{g}. \tag{2.24}$$

2.3. *Comments on different computational fluid dynamics–discrete element method models*

Clearly, from the above discussion, there are three sets of governing equations in the CFD–DEM modelling of particle–fluid flow. They correspond to those in TFM. By reference to the discussion presented in § 2.1, the relationship and applicability of these models in the CFD–DEM approach can be obtained as discussed below.

Firstly, set II is derived from set I mainly with the decomposition of particle–fluid interaction force $n\boldsymbol{f}_i$ as shown in (2.3). Physically speaking, in set II, the pressure gradient force and viscous force on particles are separated from the volumetric particle–fluid interaction force $\boldsymbol{F}_{pf}$, while set I does not. However, such a treatment will not cause any significant difference in the simulated results because they are mathematically the same, which will be verified in § 3.

Secondly, set III is a simplified form of set I under the assumption of (2.10). In the fluid governing equations, $\boldsymbol{F}_{pf}^{\text{set I}}$ and $\boldsymbol{F}_{pf}^{\text{set III}}$ represent the total volumetric particle–fluid interaction force. The difference between them is that $\boldsymbol{F}_{pf}^{\text{set I}}$ is explicit while $\boldsymbol{F}_{pf}^{\text{set III}}$ is implicit and lumps the drag force and pressure gradient force (excluding those caused by buoyancy) together, as seen in table 1. Both models are identical only when (2.10) is satisfied.

Thirdly, when comparing set III with model B in the literature, a slight difference related to the viscous part exists (Xu *et al.* 2000; Kafui *et al.* 2002; Feng & Yu 2004*a*). In the literature, the particle–fluid interaction force $\boldsymbol{F}_{pf}$ and $\boldsymbol{f}_{pf}$ in model B includes a component of the viscous force $\varepsilon_s\nabla\cdot\boldsymbol{\tau}$, but it has been excluded in the present set III. From its derivation as shown in (2.6)–(2.9), it can be seen that the viscous part together with the pressure has been hidden in the expression of $(n\boldsymbol{f}'/\varepsilon\text{-}\rho\varepsilon_s\boldsymbol{g})$ in (2.8) and (2.9).

Most importantly, it should be noted that set III is not a general model, and its application is conditional. Strictly speaking, it can be used only when (2.10) is satisfied. Alternatively, from the viewpoint of forces, the following condition obtained from (2.4) and (2.10) should be satisfied in a CFD cell:

$$\boldsymbol{F}_{resid} = \varepsilon_s\nabla\cdot\boldsymbol{\xi} - n\boldsymbol{f}'\varepsilon_s/\varepsilon_f + \rho_f\varepsilon_s\boldsymbol{g} = 0. \tag{2.25a}$$

Note that

$$\left.\begin{aligned} \varepsilon_s &= \frac{1}{\Delta V}\sum_{i=1}^{n}(V_{p,i}),\ \nabla\cdot\boldsymbol{\xi} = \frac{1}{\Delta V}\sum_{i=1}^{n}(-V_{p,i}\nabla p + V_{p,i}\nabla\cdot\boldsymbol{\tau}), \\ n\boldsymbol{f}'_i &= \frac{1}{\Delta V}\sum_{i=1}^{n}(\boldsymbol{f}_{d,i} + \boldsymbol{f}_{vm,i} + \boldsymbol{f}_{B,i} + \boldsymbol{f}_{Saff,i} + \boldsymbol{f}_{Mag,i}), \end{aligned}\right\} \tag{2.25b}$$

then (2.25*a*) can be further written as

$$\begin{aligned} \boldsymbol{F}_{resid} = \frac{1}{\Delta V}\sum_{i=1}^{n}(\boldsymbol{f}_{resid}) = \frac{1}{\Delta V}\sum_{i=1}^{n}[&-V_{p,i}\nabla p - (\boldsymbol{f}_{d,i} + \boldsymbol{f}_{vm,i} + \boldsymbol{f}_{B,i} + \boldsymbol{f}_{Saff,i} \\ &+ \boldsymbol{f}_{Mag,i})\varepsilon_s/\varepsilon_f + V_{p,i}\nabla\cdot\boldsymbol{\tau} + \rho_f V_{p,i}\boldsymbol{g}] = 0. \end{aligned} \tag{2.25c}$$

According to (2.7), the total particle–fluid interaction force in a cell should be

$$\boldsymbol{F}_{total} = \frac{1}{\Delta V}\sum_{i=1}^{n}\left(\boldsymbol{f}_{total,i}\right) = \frac{1}{\Delta V}\sum_{i=1}^{n}\left(\boldsymbol{f}_{effective,i} + \boldsymbol{f}_{resid,i}\right), \tag{2.26}$$

where $\boldsymbol{f}_{effective,i} = (\boldsymbol{f}_{d,i} + \boldsymbol{f}_{vm,i} + \boldsymbol{f}_{B,i} + \boldsymbol{f}_{Saff,i} + \boldsymbol{f}_{Mag,i})/\varepsilon_f - \rho_f V_{p,i}\boldsymbol{g}$ according to (2.24).

Strictly speaking, the fluid flow in a real particle–fluid system is non-uniform and unsteady. That is, $\boldsymbol{F}_{resid}$ calculated according to (2.25*c*) is not equal to zero. Thus, the applicability of set III can be assessed by the value of $\boldsymbol{F}_{resid}$ relative to $\boldsymbol{F}_{total}$ in (2.26). That is, a parameter η to assess the applicability of set III can be defined as

$$\eta = |\boldsymbol{f}_{resid}|/|\boldsymbol{f}_{total}| \times 100\,\%, \tag{2.27}$$

where $\boldsymbol{f}_{resid}$ and $\boldsymbol{f}_{total}$ are, respectively, the forces acting on individual particles determined by (2.25*c*) and (2.26). η for each particle in a considered system can be traced in a CFD–DEM simulation.

3. Applicability of different CFD–DEM model formulations

Three typical particle–fluid flow systems are used to test the applicability of the three models in the present simulation: fluidization, pneumatic conveying and hydrocyclones. Fluidization and pneumatic conveying have been extensively studied, therefore our focus here is to examine the reliability of the published results based on the different CFD–DEM models. A hydrocyclone gives a more complicated flow, offering a very representative example to examine the applicability of different model formulations.

To eliminate the effects of CFD–DEM algorithms and other unexpected factors on numerical results, the simulations for each particle–fluid system are carried out based on the following conditions: (i) the same CFD–DEM code except for the necessary minor changes for the implementation of different models; (ii) the same equations to calculate the particle–particle and particle–fluid interaction forces as listed in table 2, where the drag force is based on the correlation formulated by Di Felice (1994); (iii) the same initial and boundary conditions. Ideally, all simulations should be performed with one computational code. However, this is difficult to achieve at the moment. On the other hand, our aim is to examine the difference of the three models for a given system. This aim can be achieved by ensuring that the same code is used for all the models for each of the flow systems considered. This treatment can better correspond to the real application because different investigators often use different codes, although they are developed based on the same principle. The results analysis is

Forces and torques	Equations*
Normal elastic force ($\boldsymbol{f}_{cn,ij}$)	$-\frac{4}{3}E^*\sqrt{R^*}\delta_n^{3/2}\boldsymbol{n}$
Normal damping force ($\boldsymbol{f}_{dn,ij}$)	$-c_n\left(8m_{ij}E^*\sqrt{R^*\delta_n}\right)^{1/2}\boldsymbol{v}_{n,ij}$
Tangential elastic force ($\boldsymbol{f}_{ct,ij}$)	$-\mu_s\left\lvert\boldsymbol{f}_{cn,ij}\right\rvert(1-(1-\delta_t/\delta_{t,max})^{3/2})\hat{\boldsymbol{\delta}}_t\ (\delta_t < \delta_{t,max})$
Tangential damping force ($\boldsymbol{f}_{dt,ij}$)	$-c_t\left(6\mu_s m_{ij}\lvert\boldsymbol{f}_{cn,ij}\rvert\sqrt{1-\lvert\delta_t\rvert/\delta_{t,max}}/\delta_{t,max}\right)^{1/2}$ $\times\boldsymbol{v}_{t,ij}(\delta_t < \delta_{t,max})$
Coulumb friction force ($\boldsymbol{f}_{t,ij}$)	$-\mu_s\left\lvert\boldsymbol{f}_{cn,ij}\right\rvert\hat{\boldsymbol{\delta}}_t\ (\delta_t \geqslant \delta_{t,max})$
Torque by tangential forces ($\boldsymbol{M}_{t,ij}$)	$\boldsymbol{R}_{ij}\times\left(\boldsymbol{f}_{ct,ij}+\boldsymbol{f}_{dt,ij}\right)$
Rolling friction torque ($\boldsymbol{M}_{r,ij}$)	$\mu_{r,ij}\left\lvert\boldsymbol{f}_{n,ij}\right\rvert\widehat{\boldsymbol{\omega}}_{ij}^{n}$
Drag force ($\boldsymbol{f}_{d,i}$)	$0.125C_{d0,i}\rho_f\pi d_i^2\varepsilon_i^2\lvert\boldsymbol{u}_i-\boldsymbol{v}_i\rvert(\boldsymbol{u}_i-\boldsymbol{v}_i)\varepsilon_i^{-\chi}$
Pressure gradient force ($\boldsymbol{f}_{\nabla p,i}$)	$-\nabla p\cdot V_{p,i}$
Viscous force ($\boldsymbol{f}_{\nabla\cdot\boldsymbol{\tau},i}$)	$-(\nabla\cdot\boldsymbol{\tau})V_{p,i}$

where $1/m_{ij}=1/m_i+1/m_j$, $1/R^*=1/\lvert\boldsymbol{R}_i\rvert+1/\lvert\boldsymbol{R}_j\rvert$, $E^*=E/2(1-\nu^2)$, $\widehat{\boldsymbol{\omega}}_{ij}^n=\frac{\boldsymbol{\omega}_{ij}^n}{\lvert\boldsymbol{\omega}_{ij}^n\rvert}$, $\hat{\boldsymbol{\delta}}_t=\boldsymbol{\delta}_t/\lvert\boldsymbol{\delta}_t\rvert$, $\delta_{t,max}=\mu_s((2-\nu)/2(1-\nu))\delta_n$, $\boldsymbol{v}_{ij}=\boldsymbol{v}_j-\boldsymbol{v}_i+\boldsymbol{\omega}_j\times\boldsymbol{R}_j-\boldsymbol{\omega}_i\times\boldsymbol{R}_i$, $\boldsymbol{v}_{n,ij}=(\boldsymbol{v}_{ij}\cdot\boldsymbol{n})\cdot\boldsymbol{n}$, $\boldsymbol{v}_{t,ij}=(\boldsymbol{v}_{ij}\times\boldsymbol{n})\times\boldsymbol{n}$, $\chi=3.7-0.65\exp[-(1.5-\log_{10}Re_i)^2/2]$, $C_{d0,i}=(0.63+4.8/Re_i^{0.5})^2$, $Re_i=\rho_f d_{pi}\varepsilon_i\lvert\boldsymbol{u}_i-\boldsymbol{v}_i\rvert/\mu_f$, $\boldsymbol{\tau}=\mu_f[(\nabla\boldsymbol{u})+(\nabla\boldsymbol{u})^{-1}]$, $\varepsilon_i=1-\sum_{i=1}^n V_{p,i}/\Delta V$. Note that tangential forces $(\boldsymbol{f}_{ct,ij}+\boldsymbol{f}_{dt,ij})$ should be replaced by $\boldsymbol{f}_{t,ij}$ when $\delta_t\geqslant\delta_{t,max}$.

*Parameters in these equations are explained in tables 3–5.

Table 2. Components of forces and torques acting on particle *i*.

mainly carried out in terms of flow patterns, forces, and parameter η defined by (2.27). For convenience, the simulation conditions for each case are described, respectively.

The methods for the numerical solution of CFD and DEM have been well established in the literature (e.g. Xu & Yu 1997). For convenience, it is briefly described here. An explicit time integration method is used for DEM to solve the translational and rotational motions of discrete particles (Cundall & Strack 1979). The conventional semi-implicit method for pressure-linked equations (SIMPLE) method is used for CFD to solve the fluid governing equations (Patankar 1980). The governing equations are discretized in finite volume form on a uniform staggered grid. The second-order central difference scheme is used for the pressure gradient and divergence terms, the first-order up-wind scheme for the convection term, and a second-order Crank–Nicolson scheme for the time derivative. The CFD–DEM coupling scheme 3 as discussed earlier, is used in all the simulation cases. At each time step, DEM will give information, such as the positions and velocities of individual particles, for the evaluation of porosity and volumetric fluid drag force in a computational cell. CFD will then use these data to determine the gas flow field which then yields the fluid drag forces acting on individual particles. Incorporation of the resulting forces into DEM will produce information about the motion of individual particles for the next time step. All the simulations are carried out on the Intel® Xeon® CPU5130 2.0 GHz, and the simulation time varies from hours for a case of gas fluidization or pneumatic conveying to days for a case of hydrocyclones.

3.1. *Fluidization*

Fluidization is one of the most popular particle–fluid flow systems in the CFD–DEM modelling. The conflicting views, if any, about the applicability of difference model

Variables	Values
Bed geometry:	
Bed width	150 mm
Bed thickness	24 mm
Initial bed height	240 mm
Total CFD cells	15×120
Cell size ($\Delta x \times \Delta z$)	$10\,\mathrm{mm} \times 10\,\mathrm{mm}$
Particle properties:	
Number of particles (N)	15 000
Particle diameter (d_p)	4 mm
Particle density (ρ_p)	$2500\,\mathrm{kg\,m^{-3}}$
Particle–particle/wall sliding friction (μ_s)	0.4
Particle–particle/wall rolling friction (μ_r)	$1\,\%d_p$ mm
Particle–particle/wall damping ($c_n = c_t$)	0.3
Particle Young's modulus (E)	1.0×10^7 Pa
Particle Poisson ratio (ν)	0.3
Time step (Δt)	1.75×10^{-7} s
Fluid properties:	
Gas density	$1.2\,\mathrm{kg\,m^{-3}}$
Gas viscosity	1.8×10^{-5} Pa s

TABLE 3. Parameters used in the present gas fluidization.

formulations mainly stem from the study of this flow system (Hoomans *et al.* 1998; Xu & Yu 1998; Kafui *et al.* 2002, 2004; Feng & Yu 2004*a,b*; Di Renzo & Di Maio 2007). However, previous studies did not examine this issue theoretically but focused on the result comparison. The outcomes are not as general and convincing. This deficiency can be overcome with the support of the theoretical arguments presented in § 2. Therefore, as the first step to examine the applicability of different models listed in table 1, fluidization is taken as our first case study. The simulation condition is similar to that of Feng & Yu (2004*b*), but the structure used in this work has a thickness of six-particle diameter with front and rear wall boundary conditions. It should be noted that CFD for the fluid flow is assumed to be two-dimensional due to the thin bed thickness. However, DEM for the particle flow is three-dimensional. Such a technique of coupling two-dimensional CFD with three-dimensional DEM has been successfully used in the literature (e.g. Xu & Yu 1998; Kafui *et al.* 2002, 2004; Feng & Yu 2004*a,b*). It is adopted in the present study of fluidization. Table 3 lists the parameters used. It should be noted that the initial bed conditions for all the simulation cases of fluidization are identical. The bed is produced by randomly dropping particles into the rectangular box as done elsewhere (Zhou *et al.* 2009), and its porosity is 0.418.

Figure 1 shows the initial response of particles to the introduction of gas using the three models when the gas superficial velocity is 3.0 m s^{-1}. It can be observed that the flow patterns obtained are quite comparable, although the bed height generated by set III is slightly higher than those generated by sets I and II. This is consistent with the previous findings (Kafui *et al.* 2004; Feng & Yu 2004*b*). The relationship between the pressure drop and gas superficial velocity is an important feature in gas fluidization. Figure 2 shows such a relationship generated by the three models, indicating again that different model formulations do not yield any significant differences.

The examination of different particle–fluid interaction forces is useful in identifying any difference between the three models at a more fundamental level. It should be noted that the virtual mass, Basset and lift forces are not considered in all fluidization

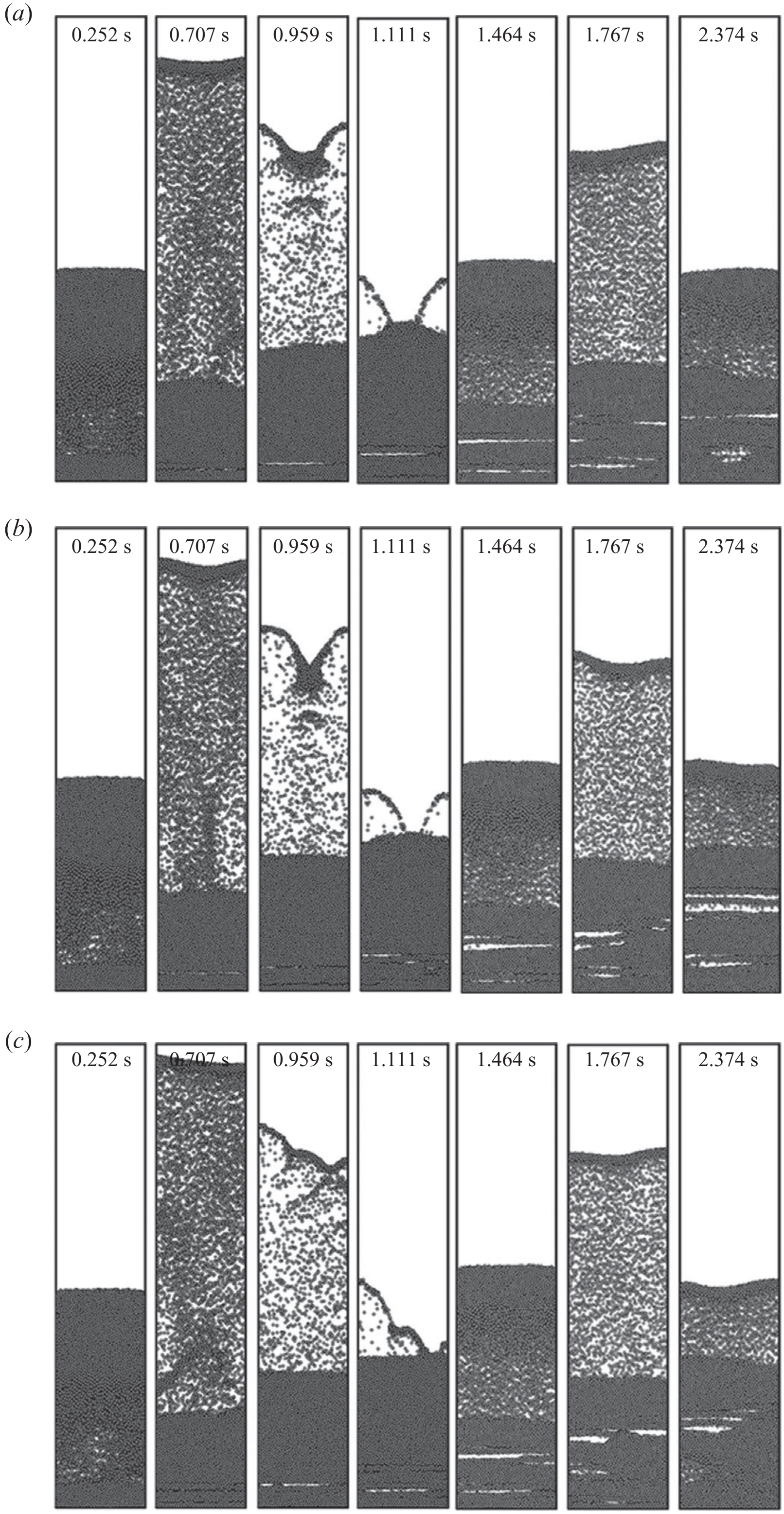

FIGURE 1. Snapshots showing the flow patterns of particles at the early stage for different CFD–DEM models when gas superficial velocity is 3.0 m s^{-1}: (*a*) set I, (*b*) set II and (*c*) set III.

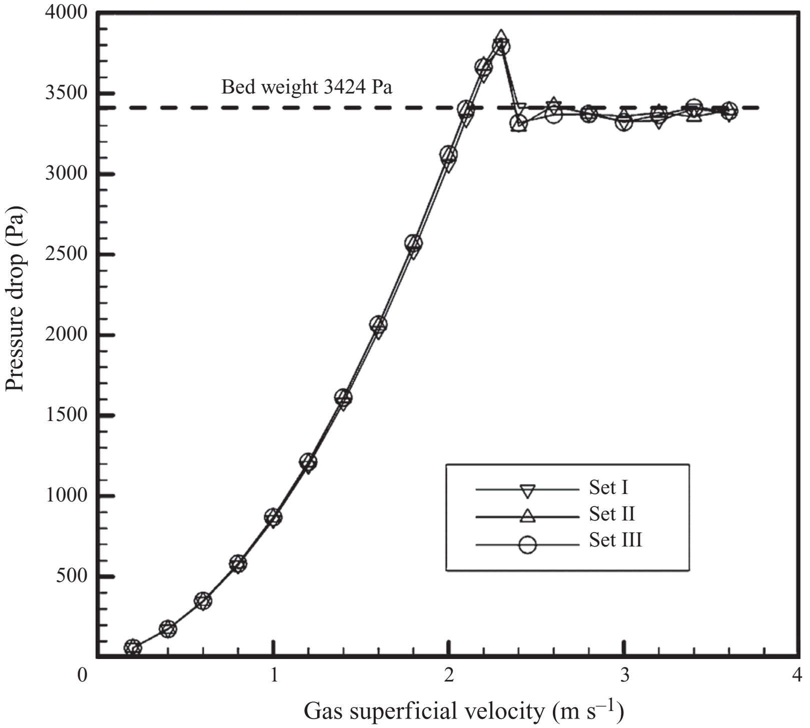

FIGURE 2. The relationship between bed pressure drop and gas superficial velocity for the three models in gas fluidization.

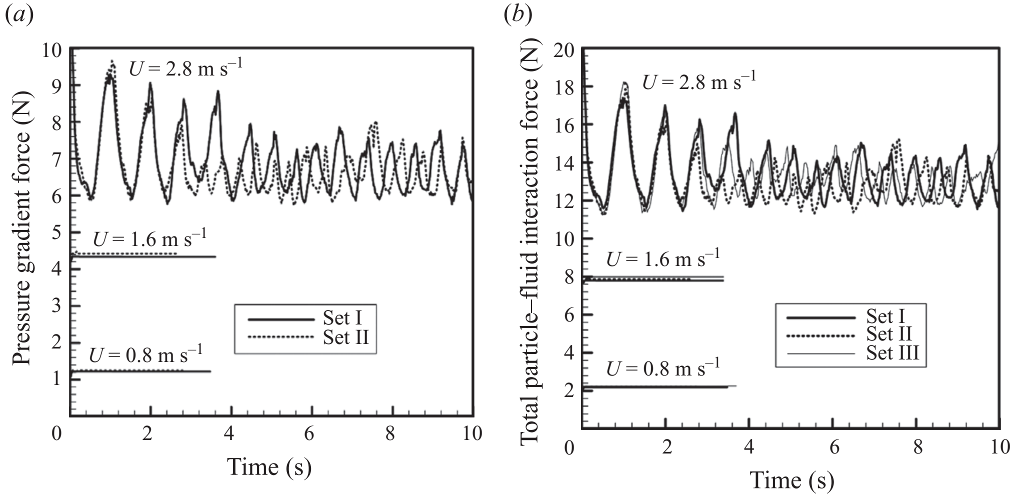

FIGURE 3. Variation of (*a*) the pressure gradient force with time for sets I and II; and (*b*) the total particle–fluid interaction force ($=\sum_{i=1}^{N}(\boldsymbol{f}_{d,i}+\boldsymbol{f}_{\nabla p,i}+\boldsymbol{f}_{\nabla\cdot\boldsymbol{\tau},i})$ for sets I & II; and $\sum_{i=1}^{N}(\boldsymbol{f}_{d,i}/\varepsilon_f-\rho_f V_{p,i}\boldsymbol{g})$ for set III) for the three models.

cases in this work, because they are insignificant compared with the pressure gradient force and drag force, particularly in gas fluidization (Crowe *et al.* 1998; Zhu *et al.* 2007). The pressure gradient force and drag force are two dominant particle–fluid interaction forces, and their variations with time are given in figure 3. As shown in figure 3(*a*), the difference in the pressure gradient force between sets I and II exists, even in the fixed bed. However, such a difference is still small, which cannot be reflected by flow patterns (figures 1*a* and 1*b*). The difference is mainly caused by the different treatments of the pressure gradient force in the model formulation and hence the numerical scheme. In set II, the pressure gradient force is incorporated into the fluid governing equations, based on the cell properties such as porosity and pressure drop. However, in set I, the pressure gradient force acting on the individual particles in a cell are summed together with the drag force. It is treated as a property on the particle scale. In theory, as discussed by Feng & Yu (2004*a*), information transfer from particle scale to cell scale is more reasonable as it can avoid the unnecessary assumption of distributing a cell property among particles. Therefore, set I should be more reliable. Figure 3(*b*) shows the total particle–fluid interaction forces (including the drag force, pressure gradient force and viscous force) for the three models in the vertical direction, thus showing some slight differences. It can be seen that the particle–fluid interaction force generated by set III is larger than the other two, explaining why the bed height from set III is slightly higher as shown in figure 1. It indicates that, in set III, the total particle–fluid interaction force represented by (2.23) is slightly overestimated. This must be caused by the assumption made in (2.10) or (2.25).

The assumption as given by (2.25) can be examined by parameter η. For each particle in the bed, the total particle–fluid interaction force $\boldsymbol{f}_{total}$ can be determined by (2.26) while the ignored force $\boldsymbol{f}_{resid}$ in set III is calculated by (2.25*c*). Thus, according to (2.27), each particle has a value of η. Figure 4(*a*) shows the variations of bed averaged η with time when gas superficial velocity is 3.4 m s^{-1}. It can be seen that η is small, fluctuating around 9 %. Figure 4(*b*) further shows a snapshot of solid flow patterns with spatial distributions of η, together with the solid and gas flow fields and porosity spatial distribution. It can be seen that large η mainly locates in areas where voids or bubbles exist, indicating a larger variation in porosity, pressure and velocity. Such a spatial variation of η can explain the observed differences of set III with other two models such as higher bed height or particle–fluid interaction force. It indicates that (2.25) is not always satisfied, particularly in those regions with gas voids and bubbles. Nevertheless, the overall differences between the three models in gas fluidization are not significant.

It should be noted that the simulation cases above are all carried out in a narrow fluidized bed. The solid flow in such a narrow bed is more one-dimensional. However, in the real fluidization process, it is featured with the formation of gas bubbles, particle clusters and rigorous two-dimensional or three-dimensional motion of particles. It is necessary to examine the effect of bed geometry on η. Thus, a case is chosen with the bed width 3 times larger than the one in table 3, and total 60 000 particles involved. Figure 5(*a*) shows the variations of bed averaged η at around 7 %, slightly smaller than that in the narrow bed (figure 4*a*). A snapshot of solid flow patterns is also shown in figure 5(*b*) with η spatial distribution, together with the corresponding solid and gas flow fields and porosity distribution. It can be seen that the large η still mainly locates in the boundary region of gas bubbles and the interface between dense and dilute particle flow regions, which is consistent with those in figure 4(*b*).

In gas fluidization, the drag force is almost equally as important as the pressure gradient force where the buoyancy force is negligible. However, in liquid fluidization, the buoyancy force becomes more important. The flow features of liquid fluidization are also different from those in gas fluidization. Thus, as part of the present study, liquid fluidization is also considered. The three models show results consistent with the gas fluidization. Thus, for brevity, they are not presented here.

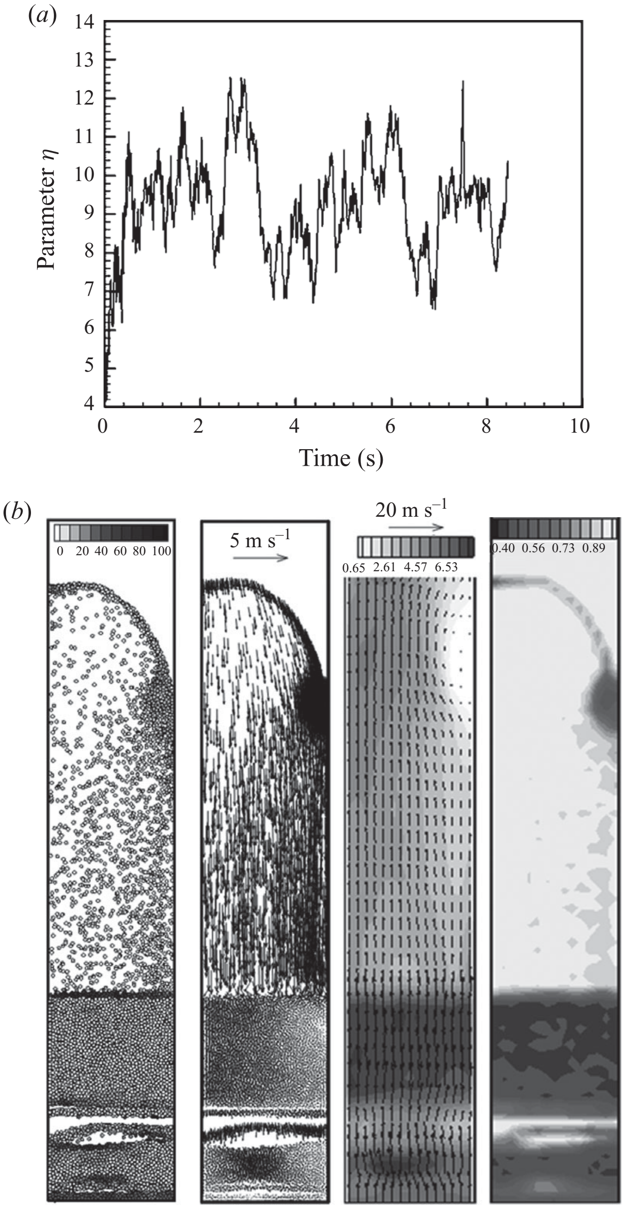

FIGURE 4. (*a*) Variations of bed averaged η when gas superficial velocity is 3.4 m s^{-1}, and (*b*) a snapshot at $t = 6.341$ s showing the solid flow patterns with spatial distribution of η, and the corresponding particle velocity field, gas flow field and porosity distribution (data are generated by set I).

Therefore, it can be concluded that the differences in the simulated results based on sets I, II and III are very small. All the three models can be applied to such a system, although theoretically set I is most acceptable. They also confirm that the results reported in the literature, produced by either set II or set III (i.e. models A or B), are reasonable.

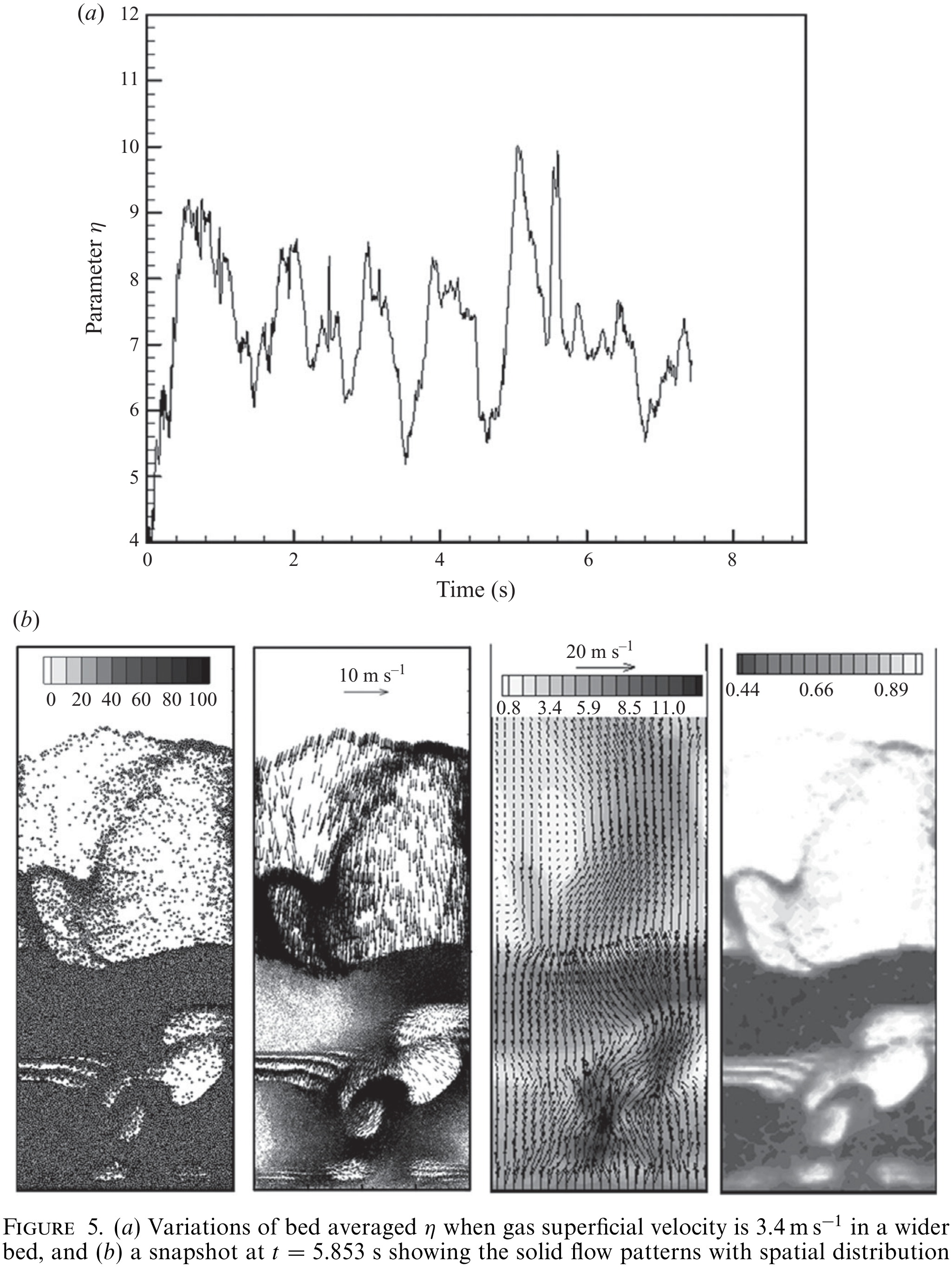

FIGURE 5. (*a*) Variations of bed averaged η when gas superficial velocity is $3.4\,\mathrm{m\,s^{-1}}$ in a wider bed, and (*b*) a snapshot at $t = 5.853$ s showing the solid flow patterns with spatial distribution of η, and the corresponding particle velocity field, gas flow field and porosity distribution (data are generated by set I).

3.2. *Pneumatic conveying*

Pneumatic conveying is one of the most commonly used methods of transporting granular materials from one place to another. Depending on solid loading and conveying speeds, one can distinguish between dilute phase, dispersed and dense

Variables	Values
Pipe geometry:	
Diameter	50 mm
Length	0.8 m
Number of body-fitted cells	$7 \times 7 \times 100$
Particle properties:	
Number of particles (N)	33 000
Particle diameter (d_p)	3 mm
Particle density (ρ_p)	1000 kg m^{-3}
Particle–particle/wall sliding friction (μ_s)	0.4
Particle–particle/wall rolling friction (μ_r)	1 %d_p mm
Particle–particle/wall damping ($c_n = c_t$)	0.1
Particle Young's modulus (E)	5.0×10^9 Pa
Particle poisson ratio (ν)	0.33
Time step (Δt)	3.8×10^{-6} s
Gas properties:	
Density	1.2 kg m^{-3}
Viscosity	1.8×10^{-5} Pa s

TABLE 4. Parameters used in the present simulation of pneumatic conveying.

phase slug flow regimes where the latter is most commonly used. To understand the fundamentals of slug flow, the CFD–DEM approach in a set II or set III format has been increasingly used in recent years (see e.g. the review of Zhu *et al.* 2008 and Kuang *et al.* 2008). It is therefore important to know the applicability of different model formulations to this system. Table 4 shows the parameters used in the present simulations of the horizontal pneumatic conveying. For computational efficiency, a 0.8 m horizontal pipe with internal diameter of 0.04 m is chosen as the computation domain, facilitated by periodic boundaries for gas and particles in the flow direction as used by Kuang *et al.* (2008). In all the simulations, the same initial particle configuration is used, which consists of a stationary slug and a stationary settled layer. The flow of both gas and solid phases is three-dimensional.

Figure 6 shows the snapshots of particle flow patterns in the slug flow regime for the three models. It can be seen that throughout the entire physical time considered, there is no significant difference in the shape of slugs, and the height of settled layers predicted by the three models. In each simulation, a slug locates at almost the same axial position in the pipe with the evolution of time. This shows that the three models predict the same slug velocity. Note that slug velocity as well as slug shape and settled layer height are the three key process parameters usually used to characterize slug flow. The variations of pressure drop with time for the three models are also traced, and shown in figure 7. It can be observed that the differences in the pressure drop generated by the three models are small. The variations of particle–fluid interaction forces in the horizontal direction are also examined and shown in figure 8. Again, it can be seen that the three models produce comparable results with negligible differences.

Figure 9(*a*) shows the spatial distribution of η. It can be seen that η is close to zero within a slug, but may have a relatively large magnitude within settled layers. This result suggests that set III is not so suitable in the simulation of inhomogeneous pneumatic conveying, such as stratified flow and dispersed flow with clusters. This is because gas mainly flows over settled layers, and its flow is non-uniform, hence

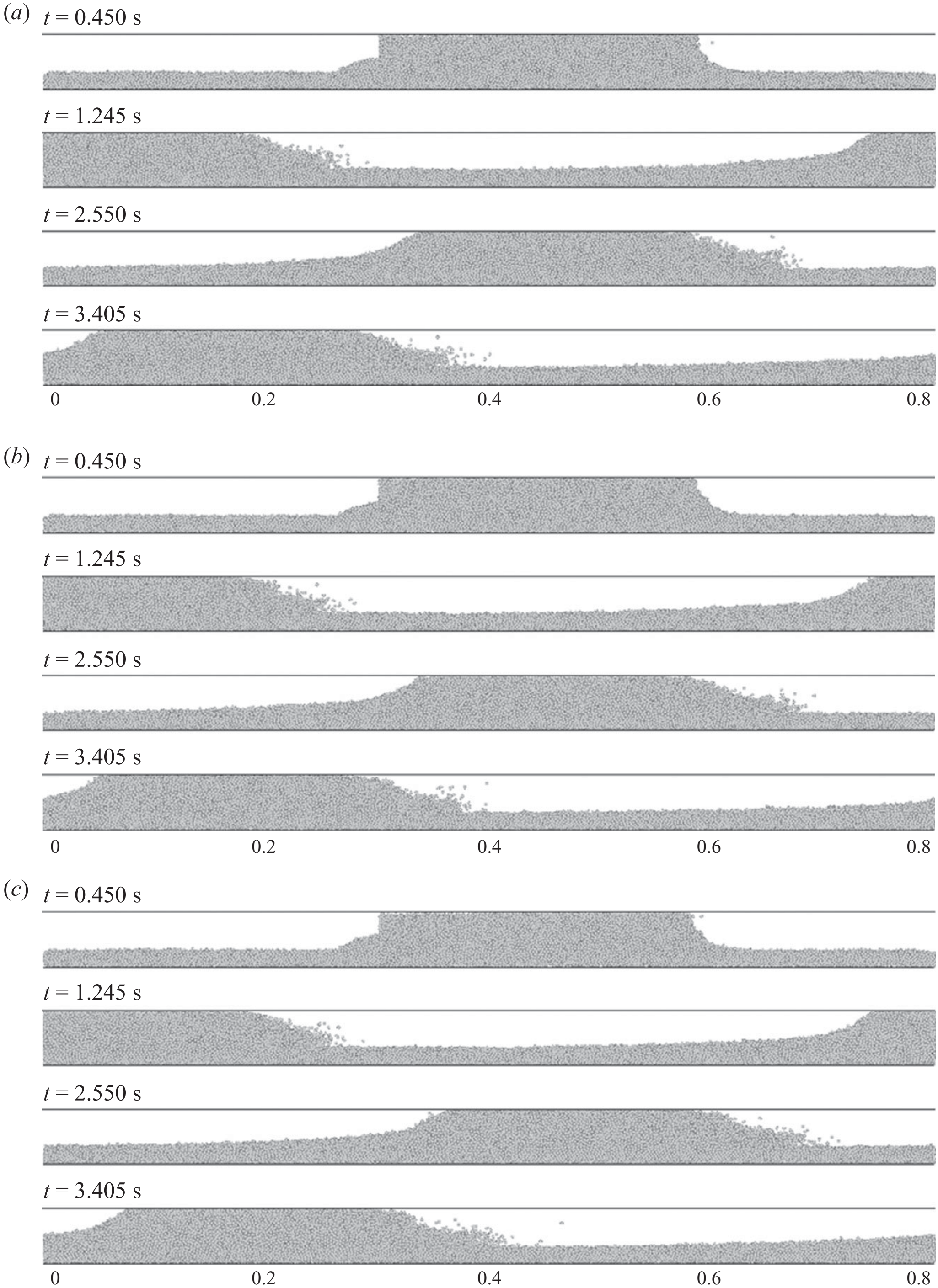

FIGURE 6. Side views of particle flow patterns in slug-flow pneumatic conveying when gas superficial velocity is 2.1 m s^{-1}, calculated by (*a*) set I, (*b*) set II and (*c*) set III.

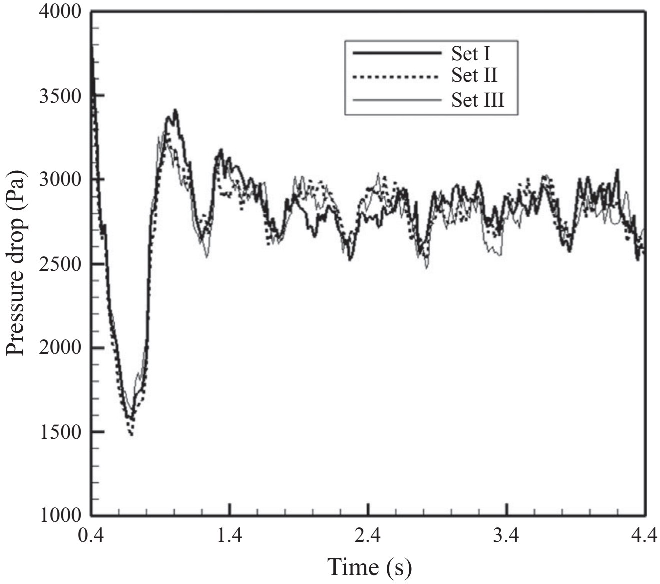

FIGURE 7. Variation of the pressure drop with time for the three models under the conditions corresponding to figure 6.

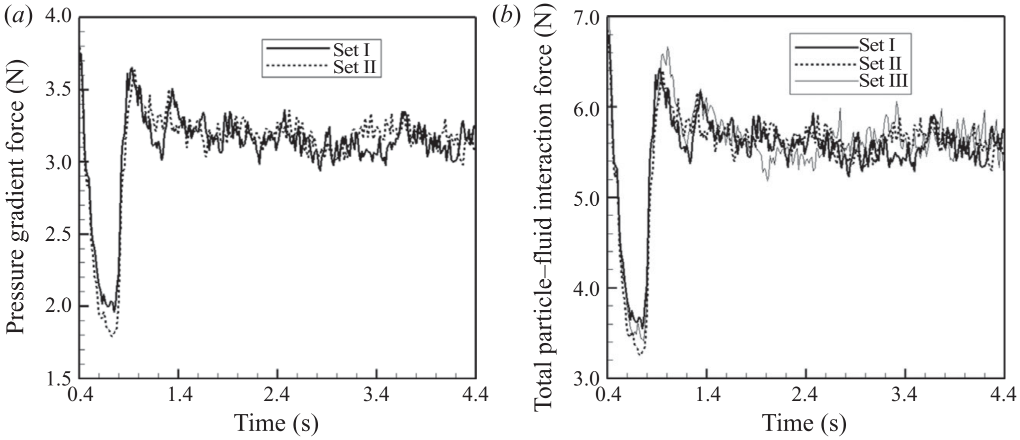

FIGURE 8. Variation of: (*a*) the pressure gradient force with time for sets I and II; and (*b*), the total particle–fluid interaction force ($= \sum_{i=1}^{N} (\boldsymbol{f}_{d,i} + \boldsymbol{f}_{\nabla p,i} + \boldsymbol{f}_{\nabla\cdot\boldsymbol{\tau},i})$ for sets I and II; and $\sum_{i=1}^{N} (\boldsymbol{f}_{d,i}/\varepsilon_f - \rho_f V_{p,i}\boldsymbol{g})$ for set III) for the three models.

the assumption induced by (2.10) or (2.25) is not satisfied. However, it is relatively uniform within a slug, as shown in figure 9(*b*). Hence, set III can be applied in this flow regime. It should be pointed out that in a slug flow, slug behaviour depends on particle motion and gas flow within a slug, e.g. the pressure drop in the whole conveying pipeline is the result of the pressure difference when gas flows across slugs, as demonstrated in figure 9(*c*). As a result, although η deviates from zero within settled layers, set III still produces gas and solid flow patterns similar to those given by sets I and II.

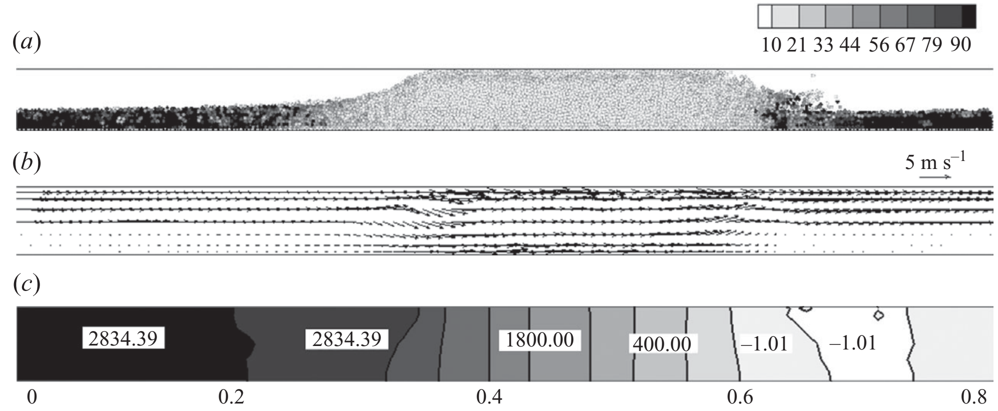

FIGURE 9. (*a*) Snapshots produced by set I showing spatial distributions of η; (*b*) gas velocity profile; (*c*) pressure drop at $x = 0.02$ m with 4 particle diameter thickness, corresponding to figure 6(*a*).

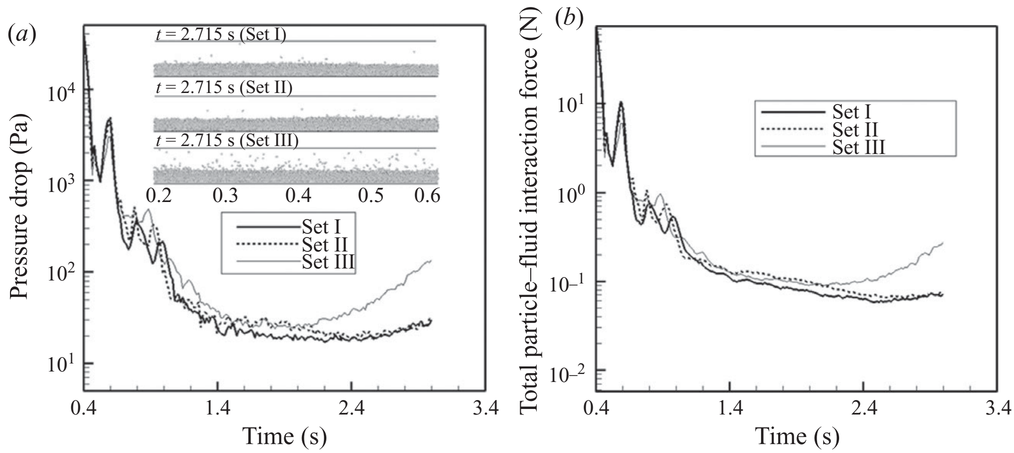

FIGURE 10. Variations of (*a*) pressure drop and (*b*) the total particle–fluid interaction force ($=\sum_{i=1}^{N}(\boldsymbol{f}_{d,i}+\boldsymbol{f}_{\nabla p,i}+\boldsymbol{f}_{\nabla\cdot\boldsymbol{\tau},i})$ for sets I and II; and $\sum_{i=1}^{N}(\boldsymbol{f}_{d,i}/\varepsilon_f-\rho_f V_{p,i}\boldsymbol{g})$ for set III) for non-slug flow when gas superficial velocity is 10 m s^{-1}. The inset in (*a*) shows a comparison of solid flow patterns for non-slug flow at one snapshot.

Figure 10 shows the variations of the pressure drop and particle–fluid interaction forces for non-slug flow when gas superficial velocity is $10\,\mathrm{m\,s^{-1}}$. It can be observed that, at the initial stage of slug collapsing, the difference is minor. However, once the flow reaches its macroscopically steady state, set III generates a relatively large pressure drop, which corresponds to a large pressure gradient force, and the motion of particles is slightly more vigorous. This indicates that set III should be used with caution when applied to the non-slug flow regimes in pneumatic conveying. It is for this reason that set I (or set II) was used in our recent studies of gas–solid flow in pneumatic conveying (Kuang, Yu & Zou 2009).

3.3. *Hydrocyclones*

A hydrocyclone separates particles in a liquid suspension or slurry (normally a mixture of water and particles) mainly according to their densities or sizes depending

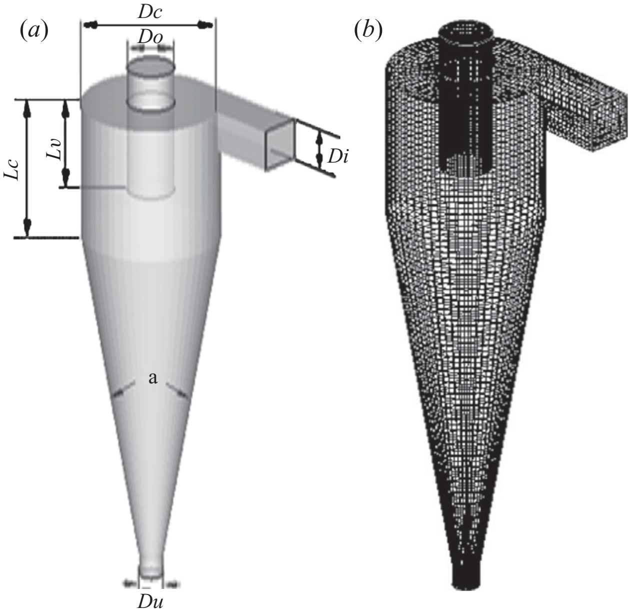

FIGURE 11. Geometry (*a*) and mesh representation (*b*) of the simulated hydrocyclone.

on operations. It is widely used in industry, particularly in mineral and chemical processing because of its simplicity in design, high capacity, low maintenance and operational cost (Svarosky 1984). The flow behaviour in a hydrocyclone is very complicated. For example, the strong rotational flow of liquid suspension can create a low-pressure axial core and a free liquid surface. Such a low-pressure core may communicate directly with the atmosphere at the outlets with air filled. The air is inhaled through the apex and forms an air core, which often results in poorer performance. Moreover, the suspension that is fed to a hydrocyclone is thickened partially by the effect of centrifugal forces. The suspension is withdrawn at the underflow with a high solid concentration, and the clarified liquid leaves the hydrocyclone by the overflow through the vortex finder. Such a complex flow is very useful in examining the applicability of the three models, particularly set III.

In this work, the particle–liquid–air flow in a hydrocyclone is simulated by both sets I and III. The diameter of the hydrocyclone considered is 75 mm and its geometry and mesh representation are shown in figure 11 and table 5. Parameters used in the DEM for the current case are also listed in table 5. Figure 11(*b*) shows the computational domain, containing 87 500 cells. The whole computational domain is divided by hexahedron grids. Trial numerical results demonstrate that the solution is independent of the characteristics of the mesh size. The pressure at the two outlets (vortex finder and apex) is set to 1 atm. The inlet water velocity and the particle velocity are both 2.25 m s^{-1}. The particle diameter is 2 mm and particle density ranges uniformly from 800 to 1200 kg m^{-3}. To better evaluate the proposed models, the fluid–solid interaction forces considered are two dominant forces, i.e. the drag force and pressure gradient force. Other fluid–solid forces such as the Basset force and lift forces are ignored because: (i) the aim of this work is to investigate the difference between sets I and III; and (ii) their effects are very minor from our trial test, but their involvement may induce uncertainty in computation (NB equations to calculate some of these forces are not yet generally established). It should also be noted that,

Variables	Values
Hydrocyclone geometry:	
Diameter of the body (Dc)	75 mm
Diameter of inlet (Di)	25 mm (same area quadrate is used)
Diameter of vortex finder (Do)	25 mm
Diameter of apex (Du)	12.5 mm
Length of cylindrical part (Lc)	75 mm
Length of vortex finder (Lv)	50 mm
Included angle (a)	20°
Particle properties:	
Solid flow rate	$20\,\mathrm{kg\,s^{-1}}$
Particle density distribution (ρ)	Uniform in the range of $800–1200\,\mathrm{kg\,m^{-3}}$
Particle diameter (d_p)	2 mm
Particle–particle/wall rolling friction (μ_r)	0.005 mm
Particle–particle/wall sliding friction (μ_s)	0.3
Poisson's ratio (ν)	0.3
Young's modulus (E)	1×10^7 Pa
Damping coefficient ($c_t = c_n$)	0.3
Particle velocity at inlet	$2.25\,\mathrm{m\,s^{-1}}$
Fluid properties:	
Gas density	$1.225\,\mathrm{kg\,m^{-3}}$
Gas viscosity	1.8×10^{-5} Pa s
Water density	$998.2\,\mathrm{kg\,m^{-3}}$
Water viscosity	0.001 Pa s
Water velocity at inlet	$2.25\,\mathrm{m\,s^{-1}}$

TABLE 5. Parameters used in the present simulation of hydrocyclone flow.

unlike the other two case studies, where the simulations are performed with in-house codes, the CFD computation for this system is based on the commercial software FLUENT, achieved by incorporating our DEM code into FLUENT through its User Defined Functions. This approach has been used in the study of fluidization and pneumatic conveying (Chu & Yu 2008). Currently, it is difficult to implement set II under the FLUENT platform. Therefore, our simulations are carried out only by sets I and III. However, as discussed in § 2, sets I and II are largely equivalent, which has been confirmed from the results of fluidization and pneumatic conveying. The other details of the CFD and DEM treatments can be found from our recent work on hydrocyclones and dense medium cyclones (Wang, Chu & Yu 2007; Chu *et al.* 2009).

Figure 12 shows the solid flow patterns. It can be seen that the flow pattern obtained from set III is quite different from that obtained from set I. There is separation of particles by density according to the results produced by set I as shown in figure 12(*a*). Heavy particles go to the spigot of the hydrocyclone and light particles go to the vortex finder of the hydrocyclone. However, such a phenomenon does not happen when set III is used, as shown in figure 12(*b*) where all particles exit from the bottom. Moreover, although the initial and boundary conditions are the same, the number of particles present in the hydrocyclone differs significantly: 5194 in the simulation by set I and 9217 by set III. These results indicate that set III cannot capture the flow features in this complicated system.

Different flow properties can also be observed, corresponding to the different solid flow patterns in figure 12. The variation of the pressure drop with time for sets I and III is first examined and shown in figure 13(*a*). The pressure drop generated by set

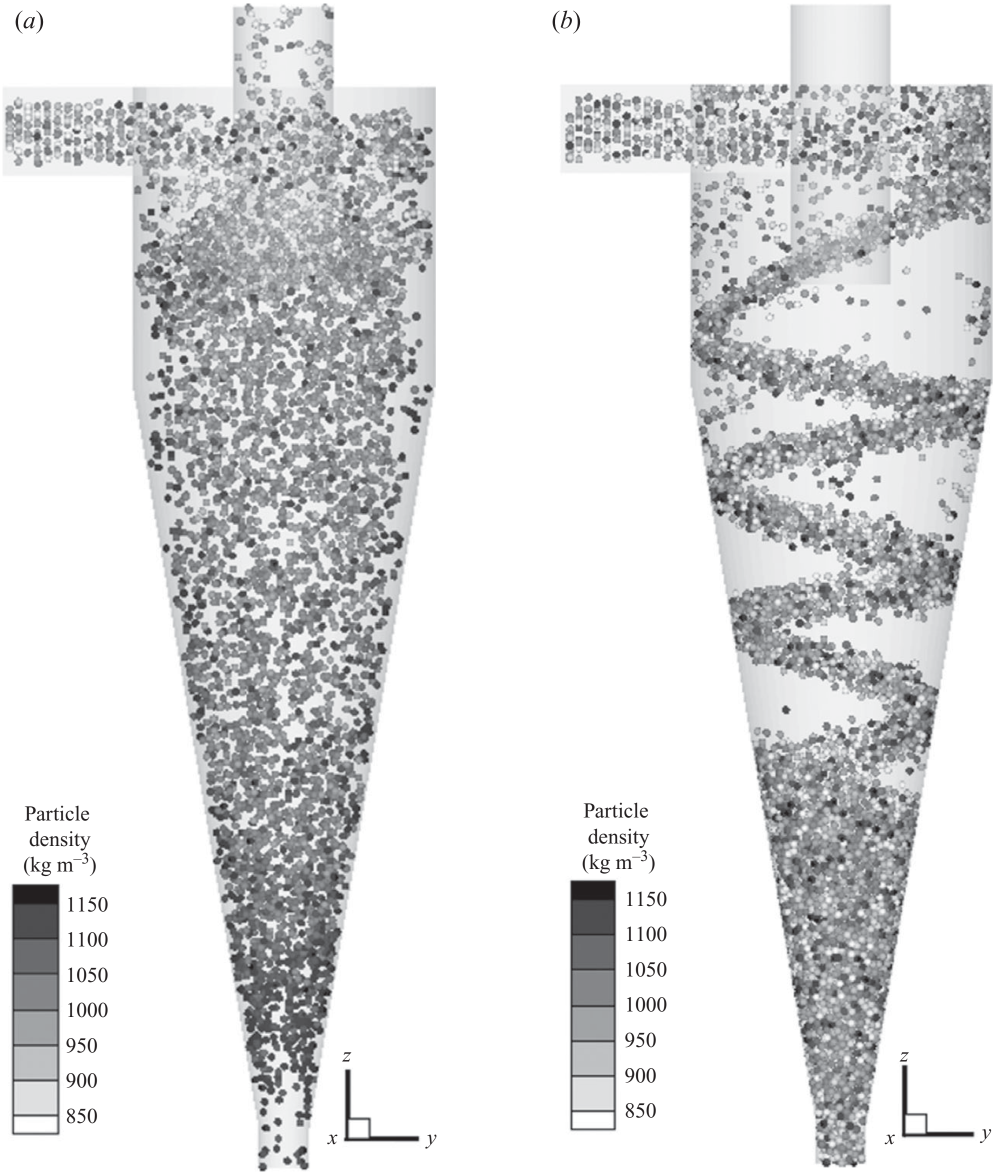

FIGURE 12. Comparison of simulated particle flow patterns in a hydrocyclone by use of different models: (*a*), set I; and (*b*), set III. Particles are coloured by particle density.

III is much lower than that generated by set I after 0.5 s. In addition, it has a large fluctuation. The total particle–fluid interaction forces, given as the sum of the pressure gradient force and the drag force on particles, are further examined and shown in figure 13(*b*). This illustrates that the total particle–fluid interaction force generated by set III is quite different from that generated by set I, and further confirms that set III is not valid in the simulation of hydrocyclone flow. The reason for this is that the assumption induced by (2.25) cannot be met for the flow in a hydrocyclone. This can be illustrated from the spatial distribution of η as shown in figure 14. The values of parameter η for almost all particles are larger than 90 %.

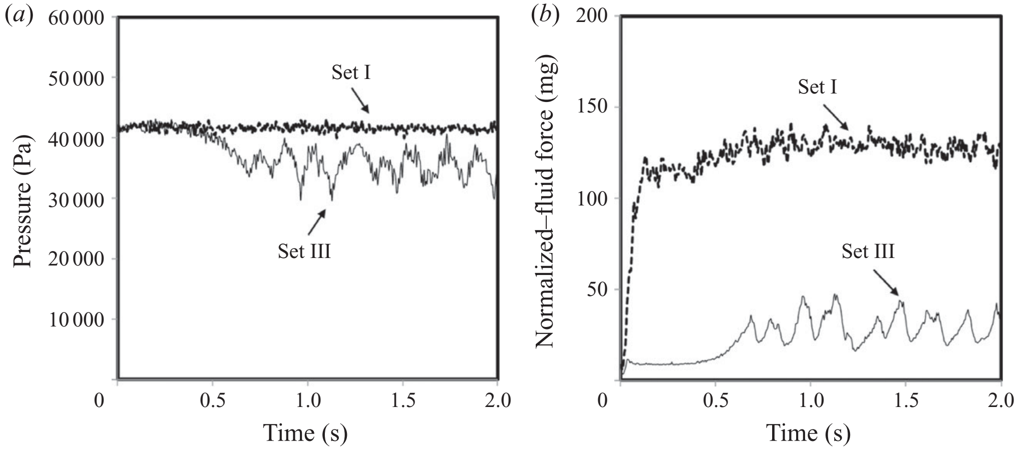

FIGURE 13. Variation of (*a*) the pressure drop with time for different model formulations, and (*b*) averaged total particle–fluid interaction force on individual particles (= $\sum_{i=1}^{N}(\boldsymbol{f}_{d,i} + \boldsymbol{f}_{\nabla p,i} + \boldsymbol{f}_{\nabla\cdot\boldsymbol{\tau},i})$ for set I; and $\sum_{i=1}^{N}(\boldsymbol{f}_{d,i}/\varepsilon_f - \rho_f V_{p,i}\boldsymbol{g})$ for set III) with time for different model formulations.

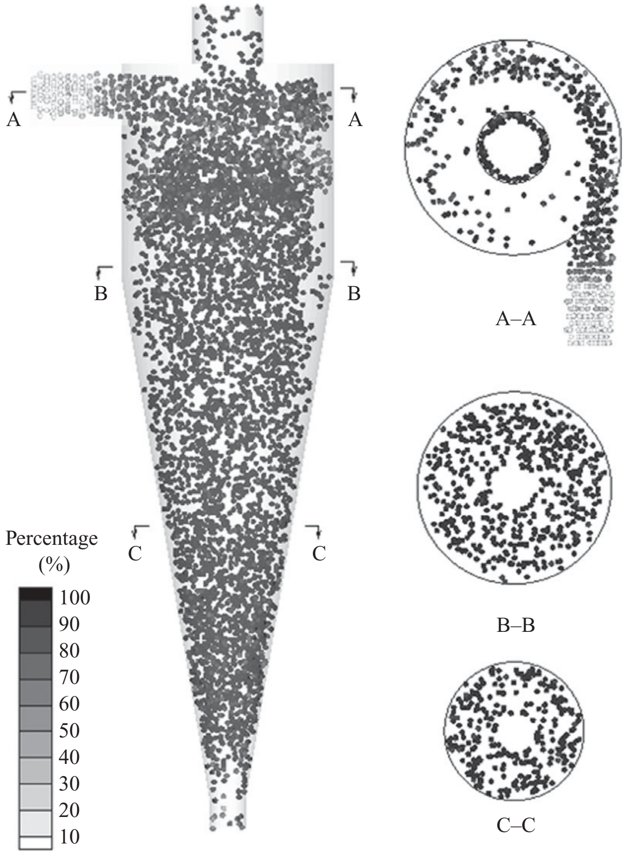

FIGURE 14. Snapshots showing the spatial distribution of η in a hydrocyclone, generated by set I.

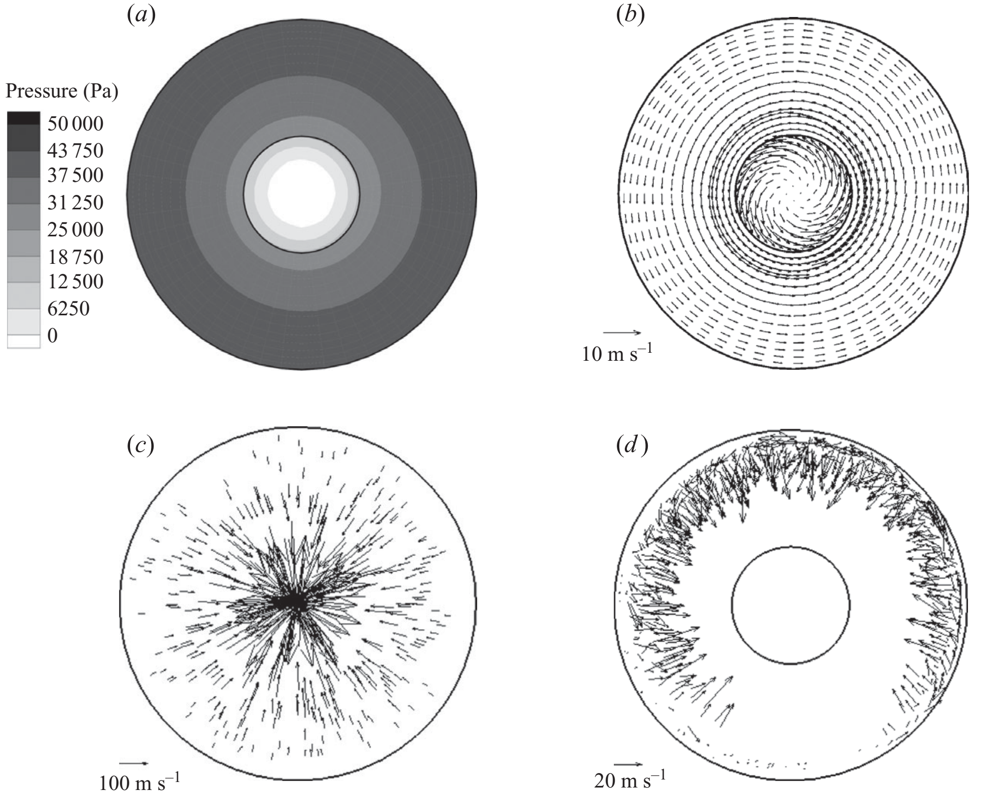

FIGURE 15. (*a*) Static pressure distribution; (*b*) velocity distribution; (*c*) vectors of total particle–fluid interaction force ($= \sum_{i=1}^{N}(\boldsymbol{f}_{d,i} + \boldsymbol{f}_{\nabla p,i})$) acting on individual particles at section B–B (figure 14) generated by set I; and (*d*) vectors of total particle–fluid interaction forces $= \sum_{i=1}^{N}(\boldsymbol{f}_{d,i}/\varepsilon_f - \rho_f V_{p,i}\boldsymbol{g})$) at the same section generated by set III. The force on a particle is normalized by dividing its weight.

It is worthwhile to examine why set III fails to predict the separation of particles by density. For this purpose, figure 15 shows the internal flow information. It can be seen from figure 15(*a*) that the pressure decreases gradually from the wall to the centre of the cyclone, indicating that the pressure gradient force will point towards the centre. On the other hand, figure 15(*b*) shows that the fluid velocity vector directs mainly tangentially. Therefore, the direction of the pressure gradient force is quite different from that of the drag force. The pressure gradient force is a radial force, and its magnitude is more than 30 times the gravity force in most of the region. This large radial force can overcome the centrifugal force and move light particles towards the centre of the cyclone where the fast upward flow can lift particles up towards the vortex finder. Figures 15(*c*) and 15(*d*) show the total particle–fluid interaction forces calculated by sets I and III, respectively. Clearly, the particle–fluid interaction force towards the centre is significantly underestimated by set III.

Generally speaking, the difference between sets I and III lies in the different treatment of the particle–fluid interaction forces. According to (2.21), each type of particle–fluid interaction force has been explicitly considered in set I, including the pressure gradient force and the drag force, which are dominant for many particle–fluid flow systems. However, as implied in (2.23), the pressure gradient force, whereby the buoyancy force is excluded, and the drag force are lumped together in set III. This treatment is not so problematic when the two forces act in the same direction. In fluidization or pneumatic conveying, the particle–fluid flow is largely one-dimensional. Consequently, sets I and III do not show any significant differences, although the conditions of (2.10) or (2.25) are not always met locally, e.g. in the areas with voids or bubbles in fluidization or the non-plug flow regime in pneumatic conveying. However, the flow in a hydrocyclone is much more complicated and truly three-dimensional for fluid and solid phases. In particular, the pressure gradient and drag forces act in different directions. Consequently, the conditions of (2.10) or (2.25) cannot be met globally or locally, and set III fails to predict the particle–fluid flow and hence the separation performance in a hydrocyclone.

Therefore, caution must be taken in applying set III in particle–fluid flow modelling. In spite of the success in the previous studies of fluidization and pneumatic conveying reported in the literature, set III should not be used in the future CFD–DEM modelling of particle–fluid flow. This consideration equally applies to the so-called model B in the TFM approach in the literature. In other words, for general application, model B should be replaced by its origin, i.e. set I as given by (2.1) and (2.2).

4. Conclusions

There are three, rather than two, models in the continuum description of particle–fluid flow, including set I, given by (2.1) and (2.2), set II, given by (2.4) and (2.5), and set III given by (2.8) and (2.9). Sets I and II result from different treatments of the fluid stress tensor term in the original equation, but they are essentially the same. Set III is however a simplified version of set I, obtained when the condition of (2.10) is met. Consequently, the application of set III is conditional.

Corresponding to the continuum treatments, there are also three sets of formulations in CFD–DEM modelling, as listed in table 1. However, unlike the continuum approach, there is a difference between sets I and II because CFD and DEM are modelled at different length scales. In theory, set I is more logical and hence more acceptable. The implementation of set II needs to implement a method to distribute (some of) the particle–fluid forces among the particles in a CFD cell, which may induce a difference in the simulated results. However, the difference is small, and can be treated as a numerical error. Therefore, set II and, in particular, set I, which is somehow forgotten in the literature, are recommended for future CFD–DEM modelling. The application of set III is, however, conditional. Strictly speaking, it is only valid when the condition described by (2.10) or (2.25) is met, which means that fluid flow is steady and uniform or the residual force acting on particles is zero.

A new index resulting from the theoretical analysis, given by (2.27), is proposed to assess the applicability of model formulation. The test cases show that the three models are all applicable to fluidization and to a large extent, pneumatic conveying, the two systems studied most extensively thus far in the literature. The results produced by set III in the previous studies are therefore valid, although there are some minor differences when comparing with those produced by set I or set II. However, caution must be taken when applying set III to complicated flow systems like hydrocyclones, where the condition of (2.10) or (2.25) cannot be met globally or locally. In spite of its successful application reported in the literature, set III should not be used in the future work.

The authors are grateful to the Australian Research Council for the financial support of this work.

REFERENCES

Anderson, T. B. & Jackson, R. 1967 A fluid mechanical description of fluidized beds. *Ind. Engng Chem. Fundam.* **6**, 527–539.

Arastoopour, H. 2001 Numerical simulation and experimental analysis of gas/solid flow systems: 1999 Fluor–Daniel Plenary Lecture. *Powder Technol.* **119**, 59–67.

Arastoopour, H. & Gidaspow, D. 1979 Vertical pneumatic conveying using four hydrodynamic models. *Ind. Engng Chem. Fundam.* **18**, 123–130.

Beetstra, R., van der Hoef, M. A. & Kuipers, J. A. M. 2007 Numerical study of segregation using a new drag force correlation for polydisperse systems derived from lattice-Boltzmann simulations. *Chem. Engng Sci.* **62**, 246–255.

Bouillard, J. X., Lyczkowski, R. W. & Gidaspow, D. 1989 Porosity distributions in a fluidized-bed with an immersed obstacle. *AIChE J.* **35**, 908–922.

Campbell, C. S. 2006 Granular materials flows: an overview. *Powder Technol.* **162**, 208–229.

Chu, K. W. & Yu, A. B. 2008 Numerical simulation of complex particle–fluid flows. *Powder Technol.* **179**, 104–114.

Chu, K. W., Wang, B., Yu, A. B. & Vince, A. 2009 CFD–DEM modelling of multiphase flow in dense medium cyclones. *Powder Technol.* **193**, 235–247.

Crowe, C. T., Sommerfeld, M. & Tsuji, Y. 1998 *Multiphase Flow with Droplets and Particles.* CRC.

Cundall, P. A. & Strack, O. D. L. 1979 A discrete numerical model for granular assemblies. *Geotechnique* **29**, 47–65.

Di Felice, R. 1994 The voidage function for fluid–particle interaction systems. *Intl J. Multiph. Flow* **20**, 153–159.

Di Renzo, A. & Di Maio, F. P. 2007 Homogeneous and bubbling fluidization regimes in DEM–CFD simulations: hydrodynamic stability of gas and liquid fluidized beds. *Chem. Engng Sci.* **62**, 116–130.

Enwald, H., Peirano, E. & Almstedt, A. E. 1996 Eulerian two-phase flow theory applied to fluidization. *Intl J. Multiph. Flow* **22**, 21–66.

Ergun, S. 1952 Fluid flow through packed columns. *Chem. Engng Process.* **48**, 89–94.

Feng, Y. Q., Xu, B. H., Zhang, S. J., Yu, A. B. & Zulli, P. 2004 Discrete particle simulation of gas fluidization of particle mixtures. *AIChE J.* **50**, 1713–1728.

Feng, Y. Q. & Yu, A. B. 2004*a* Assessment of model formulations in the discrete particle simulation of gas–solid flow. *Ind. Engng Chem. Res.* **43**, 8378–8390.

Feng, Y. Q. & Yu, A. B. 2004*b* Comments on 'Discrete particle-continuum fluid modelling of gas-solid fluidised beds' by Kafui *et al.* [*Chem. Engng Sci.* **57** (2002) 2395–2410]. *Chem. Engng Sci.* **59**, 719–722.

Feng, Y. Q. & Yu, A. B. 2007 Microdynamic modelling and analysis of the mixing and segregation of binary mixtures of particles in gas fluidization. *Chem. Engng Sci.* **62**, 256–268.

Gidaspow, D. 1994 *Multiphase Flow and Fluidization.* Academic.

Goldhirsch, I. 2008 Introduction to granular temperature. *Powder Technol.* **182**, 130–136.

Hoomans, B. P. B., Kuipers, J. A. M., Briels, W. J. & van Swaaij, W. P. M. 1998 Comments on the paper 'Numerical simulation of the gas–solid flow in a fluidized bed by combining discrete particle method with computational fluid dynamics'. *Chem. Engng Sci.* **53**, 2645–2646.

Iddir, H., Arastoopour, H. & Hrenya, C. M. 2005 Analysis of binary and ternary granular mixtures behavior using the kinetic theory approach. *Powder Technol.* **151**, 117–125.

Ishii, M. 1975 *Thermo-Fluid Dynamics Theory of Two-Phase Flow.* Eyrolles.

Jackson, R. 1963 The mechanics of fluidized beds. Part I. The stability of the state of uniform fluidization. *Trans. Inst. Chem. Engng* **41**, 13–21.

Jackson, R. 1997 Locally averaged equations of motion for a mixture of identical spherical particles and Newtonian fluid. *Chem. Engng Sci.* **52**, 2457–2469.

Kafui, K. D., Thornton, C. & Adams, M. J. 2002 Discrete particle-continuum fluid modelling of gas–solid fluidised beds. *Chem. Engng Sci.* **57**, 2395–2410.

Kafui, K. D., Thornton, C. & Adams, M. J. 2004 Reply to comments by Feng and Yu on 'Discrete particle-continuum fluid modelling of gas–solid fluidised beds' by Kafui *et al. Chem. Engng Sci.* **59**, 723–725.

Kuang, S. B., Chu, K. W., Yu, A. B., Zou, Z. S. & Feng, Y. Q. 2008 Computational investigation of horizontal slug flow in pneumatic conveying. *Ind. Engng Chem. Res.* **47**, 470–480.

Kuang, S. B., Yu, A. B. & Zou, Z. S. 2009 Computational study of flow regimes in vertical pneumatic conveying. *Ind. Engng Chem. Res.* **48**, 6846–6858.

Lee, W. H. & Lyczkowski, R. W. 2000 The basic character of five two-phase flow model equation sets. *Intl. J. Numer. Meth. Fluids* **33**, 1075–1098.

Li, J. H. 2000 Compromise and resolution: exploring the multi-scale nature of gas–solid fluidization. *Powder Technol.* **111**, 50–59.

Lyczkowski, R. W. 1978 Transient propagation behavior of two-Phase flow equations. In *Heat Transfer: Research and Application* (ed. J. C. Chen), AIChE Symposium Series, vol. 75, Issue 174, pp. 175–174. American Institute of Chemical Engineers, New York.

Nakamura, K. & Capes, C. E. 1973 Vertical pneumatic conveying: theoretical study of uniform and annular particle flow models. *Can. J. Chem. Engng* **51**, 39–46.

Patankar, S. V. 1980 *Numerical Heat Transfer and Fluid Flow*. Hemisphere.

Prosperetti, A. & Tryggvason, G. 2007 *Computational Methods for Multiphase Flow*. Cambridge University Press.

Rudinger, G. & Chang, A. 1964 Analysis of nonsteady 2-phase flow. *Phys. Fluids* **7**, 1747–1754.

Svarovsky, L. 1984 Hydrocyclones. Technomic Publishing Inc.

Tsuji, Y. 2007 Multi-scale modeling of dense phase gas-particle flow. *Chem. Engng Sci.* **62**, 3410–3418.

Villermaux, J. 1996 New horizons in chemical engineering. In *Proceedings of the Fifth World Congress of Chemical Engineering*, San Diego, CA, pp. 16–23.

van Wachem, B. G. M., Schouten, J. C., van den Bleek, C. M., Krishna, R. & Sinclair, J. L. 2001 Comparative analysis of CFD models of dense gas–solid systems. *AIChE J.* **47**, 1035–51.

Wang, B., Chu, K. W. & Yu, A. B. 2007 Numerical study of particle–fluid flow in a hydrocyclone. *Ind. Engng Chem. Res.* **46**, 4695–4705.

Wen, C. Y. & Yu, Y. H. 1966 Mechanics of fluidization. *AIChE Ser.* **62**, 100.

Xu, B. H. & Yu, A. B. 1997 Numerical simulation of the gas–solid flow in a fluidized bed by combining discrete particle method with computational fluid dynamics. *Chem. Engng Sci.* **52**, 2785–2809.

Xu, B. H. & Yu, A. B. 1998 Comments on the paper 'Numerical simulation of the gas–solid flow in a fluidized bed by combining discrete particle method with computational fluid dynamics': reply. *Chem. Engng Sci.* **53**, 2646–2647.

Xu, B. H., Yu, A. B., Chew, S. J. & Zulli, P. 2000 Numerical simulation of the gas–solid flow in a bed with lateral gas blasting. *Powder Technol.* **109**, 13–26.

Yu, A. B. 2005 Powder processing: models and simulations. In *Encyclopedia of Condensed Matter Physics* (ed. F. Bassani, G. L. Liedl & P. Wyder), Chapter 5 56, vol. 4, pp. 401–414. Elsevier.

Zhou, Y. C., Wright, B. D., Yang, R. Y., Xu, B. H. & Yu, A. B. 1999 Rolling friction in the dynamic simulation of sandpile formation. *Physica* A **269**, 536–553.

Zhou, Z. Y., Yu, A. B. & Zulli, P. 2009 Particle scale study of heat transfer in packed and bubbling fluidized beds. *AIChE J.* **55**, 868–884.

Zhu, H. P., Zhou, Z. Y., Yang, R. Y. & Yu, A. B. 2007 Discrete particle simulation of particulate systems: theoretical developments. *Chem. Engng Sci.* **62**, 3378–3396.

Zhu, H. P., Zhou, Z. Y., Yang, R. Y. & Yu, A. B. 2008 Discrete particle simulation of particulate systems: a review of major applications and findings. *Chem. Engng Sci.* **63**, 5728–5770.